BRNO UNIVERSITY OF TECHNOLOGY
VYSOKÉ UČENÍ TECHNICKÉ V BRNĚ

FACULTY OF MECHANICAL ENGINEERING
INSTITUTE OF PHYSICAL ENGINEERING

FAKULTA STROJNÍHO INŽENÝRSTVÍ
ÚSTAV FYZIKÁLNÍHO INŽENÝRSTVÍ

ORDERED AND DISORDERED ARRAYS OF COLLOIDAL NANOPARTICLES FOR BIOMOLECULE DETECTION

USPOŘÁDANÁ A NEUSPOŘÁDANÁ POLE KOLOIDNÍCH NANOČÁSTIC A JEJICH VYUŽITÍ PRO DETEKCI BIOMOLEKUL

MASTER'S THESIS
DIPLOMOVÁ PRÁCE

AUTHOR
AUTOR PRÁCE
Bc. FILIP LIGMAJER

SUPERVISOR
VEDOUCÍ PRÁCE
Ing. MIROSLAV KOLÍBAL, Ph.D.

BRNO 2013

Vysoké učení technické v Brně, Fakulta strojního inženýrství

Ústav fyzikálního inženýrství
Akademický rok: 2012/2013

ZADÁNÍ DIPLOMOVÉ PRÁCE

student(ka): Bc. Filip Ligmajer

který/která studuje v **magisterském navazujícím studijním programu**

obor: **Fyzikální inženýrství a nanotechnologie (3901T043)**

Ředitel ústavu Vám v souladu se zákonem č.111/1998 o vysokých školách a se Studijním a zkušebním řádem VUT v Brně určuje následující téma diplomové práce:

Uspořádaná a neuspořádaná pole koloidních nanočástic a jejich využití pro detekci biomolekul

v anglickém jazyce:

Ordered and disordered arrays of colloidal nanoparticles for biomolecule detection

Stručná charakteristika problematiky úkolu:

Detekce biomolekul (např. řetězců DNA) má zasadní využití v medicíně a biologii. Současné sensory jsou často založeny na plazmonice (např. detekce pomocí hranolu), kdy jsou hledané molekuly zachytávány na často předem funkcionalizovaném povrchu zlata. Zvýšení citlivosti detekce je možní několika způsoby, např. použitím odlišného detekčního systému nebo strukturovaného aktivního povrchu (zvětšení detekční plochy). Diplomantovým úkolem bude zvolit vhodný systém pro detekci a testovat detekční citlivost tohoto systému.

Cíle diplomové práce:

1. Měření optické odezvy vzorku zlatých/stříbrných nanočástic na povrchu křemíku pomocí elipsometrie.
2. Testování použití reflektometrie k měření optické odezvy.
3. Příprava uspořádaných polí nanočástic a jejich optická měření.
4. Výběr vhodného systému a testování detekce vybraných biomolekul.

Seznam odborné literatury:

[1] Jin, Y. Engineering Plasmonic Gold Nanostructures and
Metamaterials for Biosensing and Nanomedicine. Advanced Materials 24 (2012) 5153.

[2] Giljohann D. A. et al., Gold Nanoparticles for Biology and Medicine. Angewandte Chemie International Edition 49 (2010) 4280.

[3] Saha K. et al., Gold Nanoparticles in Chemical and Biological Sensing. Chemical Reviews 112 (2012) 2739.

Vedoucí diplomové práce: Ing. Miroslav Kolíbal, Ph.D.

Termín odevzdání diplomové práce je stanoven časovým plánem akademického roku 2012/2013.

V Brně, dne 22.11.2012

L.S.

prof. RNDr. Tomáš Šikola, CSc. Ředitel ústavu	prof. RNDr. Miroslav Doupovec, CSc., dr. h. c. Děkan fakulty

ABSTRACT

This thesis deals with guided self-assembly of gold nanoparticles from their colloidal solutions onto silicon substrates and possible employment of nanoparticles for detection of biomolecules. It was found that by adjustment of solution pH and surface chemistry modification by means of electron beam irradiation it is possible to facilitate nanoparticle deposition to patterns with almost single particle precision. Spectroscopic ellipsometry was then employed in analysis of self-assembled layers of nanoparticles and its combination with a theory of effective medium approximation has proven the ability to assess nanoparticle dimensions and volume fractions. By experiments with thiolated oligonucleotides it has been shown that using ellipsometry one can detect even with very subtle changes in nanoparticle environment caused by biomolecules, thus promising its possible use in the field of biodetection.

KEYWORDS

metallic nanoparticles, colloidal gold, silicon, spectroscopic ellipsometry, biodetection, oligonucleotides, self-assembly

ABSTRAKT

Tato práce se zabývá depozicí zlatých nanočástic na křemíkové povrchy pomocí řízeného uspořádávání z jejich koloidních roztoků a možným uplatněním nanočástic v detekci biomolekul. Bylo ukázáno, že upravením pH roztoku a modifikací povrchových chemických skupin pomocí expozice vzorku elektronovým svazkem je možné dosáhnout depozice nanočástic do polí s velkou přesností. Spektroskopická elipsometrie byla poté využita k analýze připravených vrstev nanočástic a její kombinace s teorií efektivních prostředí prokázala schopnost určit rozměry nanočástic a jejich koncentraci na povrchu. Za pomocí experimentů s thiolovanými oligonukleotidy bylo ukázáno, že s pomocí elipsometrie lze detekovat i malé změny v okolí nanočástic způsobené přítomností biomolekul, což může umožnit její využití v oblasti biodetekce.

KLÍČOVÁ SLOVA

kovové nanočástice, koloidní zlato, křemík, spektroskopická elipsometrie, biodetekce, oligonukleotidy, samouspořádávání

LIGMAJER, F.: *Uspořádaná a neuspořádaná pole koloidních nanočástic a jejich využití pro detekci biomolekul.* Brno: Vysoké učení technické v Brně, Fakulta strojního inženýrství, 2013. 62 s. Vedoucí práce Ing. Miroslav Kolíbal, Ph.D.

Prohlašuji, že jsem tuto diplomovou práci vypracoval samostatně, pouze za odborného vedení Ing. Miroslava Kolíbala, Ph.D., a že veškeré podklady, ze kterých jsem čerpal, jsou uvedeny v seznamu použité literatury.

Bc. Filip Ligmajer

Děkuji Miroslavu Kolíbalovi za příležitost pracovat pod jeho vedením a za všechny cenné rady, které jsem od něj obdržel. Poděkování patří také Jiřímu Spoustovi a Janu Čechalovi za pozorné přečtení textu a mnoho užitečných připomínek, a také všem, kteří na Ústavu fyzikálního inženýrství vytvářejí tak báječnou atmosféru.

Zvláštní poděkování patří mým rodičům, bez jejichž podpory během celého studia by tato práce nemohla vzniknout, a mé přítelkyni za trpělivost a lásku.

CONTENTS

1 Introduction **3**

2 Gold nanoparticles **5**

2.1 Preparation of nanoparticles 5

2.2 Surface properties of nanoparticles 6

2.3 Self-assembly of gold nanoparticles onto solid substrates 9

2.4 Guided assembly of nanoparticles 12

2.5 Patterning of silicon substrates by electron beam 14

3 Optical properties of metallic nanostructures **23**

3.1 Theory of scattering by small particles 23

3.2 Limitations of Mie's theory 25

3.3 Optical properties of nanoparticle ensembles 27

3.4 Effective medium theory in characterization of metallic nanoparticles 29

3.5 Spectroscopic ellipsometry 30

3.6 Analysis of films of metallic nanoparticles by ellipsometry 32

4 Biosensors **37**

4.1 Plasmonics-based biosensors 37

4.2 Bioconjugation strategies for gold nanoparticles 39

4.3 Ellipsometric detection of oligonucleotides 42

5 Conclusions **47**

Bibliography **51**

List of Abbreviations **61**

A Refractive index of gold used in ellipsometry fitting **62**

1 INTRODUCTION

Gold nanoparticles (AuNPs) have received much attention in recent years due to their distinct physical and chemical attributes that make them excellent scaffolds for whole range of technological and medical applications. They provide high surface-to-volume ratio with excellent biocompatibility and also possess unique optical properties in terms of extremely high extinction coefficient, environment-dependent colour, and excellent fluorescence quenching ability, which makes them favoured components for biosensor development [1]. Moreover, some of these properties can be easily tuned by varying AuNP size, shape, or surrounding environment [2].

Although colloidal solutions of nanoparticles have been utilized in great variety of applications, it seems beneficial to deposit the nanoparticles on solid substrates and to control their density and precise position. Possible applications of nanoparticles immobilized on surfaces include enhancement of the efficiency of solar cells [3], selective growth of nanowires [4] and, especially, the rapidly developing field of nanophotonics [5].

Despite the fact that natural thermodynamic and chemical barriers often hinder the self-assembly of nanoparticles onto solid substrates, various procedures have been developed to achieve this goal. Unfortunately, these often involve rather complicated steps and also major modifications of either solid substrate or nanoparticle surface: typically applying a thick polymer coating or a layer of self-assembled alkoxysilane molecules [6]. Even more complicated are methods for guided metallic nanoparticles assembly, usually requiring some additional steps in terms of surface topography or chemical modification. These methods have proven to be valuable and in fact in many applications those interlayers do not impair the desired application. But as the field is aiming towards devices and techniques with even better sensitivity, these may turn out to be hindrance.

In the first chapter of this thesis a simple procedure leading to self-assembly of AuNPs onto silicon substrates is shown. It is based on intentional modification of colloidal solution pH. Key factors playing a major role in this approach are described and its ability to cover the surface with high concentration of nanoparticles ($> 300\,\mu m^{-2}$) is demonstrated. Extending the work published recently by our group [7] using ions, a very powerful method for *guided* self-assembly is introduced as well, employing silicon substrates pre-patterned by electron beams. These procedures for fabrication of both ordered and disordered arrays of nanoparticles are free of any interfacial layers or complex surface modification by chemicals. Only bare silicon surface and low energy electron beam is necessary to achieve nanoparticle assembly with almost single-nanoparticle precision.

The next chapter deals with extraordinary optical properties of metallic nanostructures which arise from their ability to support resonant excitations of coupled optical fields and electron oscillations, that is surface plasmon resonances (SPRs). The basis for analysis of films of metallic nanoparticles is established by combining spectroscopic ellipsometry with a theory of effective media approximations (EMA). Important characteristics of AuNP films, such as their dimensions or volume fractions, are assessed by this combination of measurement and theoretical modelling.

Last chapter is devoted to a possible application of metallic nanoparticles — the plasmonics-based detection of biomolecules, or simply plasmonic biosensing. Despite employment of metallic films which dominates the field, nanoparticles have been proposed to be valuable system as well. For example, the binding event between the recognition element and some analyte (substance of interest in an analytical procedure) can alter plasmon resonance absorption, sample conductivity, etc., which in turn can generate a detectable response signal.

Application of spectroscopic ellipsometry in the field of plasmonic biosensing is demonstrated by an experiment involving functionalization of AuNP layers by thiolated oligonucleotides and their subsequent detection using an ellipsometer. Even though further evaluation of reliability and accuracy of this method should be performed, the outcomes suggest that this biosensing scheme is sensitive enough to detect subtle changes on the nanoparticle surface and thus may be possibly incorporated in next generation of healthcare devices.

2 GOLD NANOPARTICLES

Gold nanoparticles (AuNPs) play a particularly important role in nanotechnology because they are ideal for interfacing with biomolecules and cells. AuNPs are available in large quantities with excellent shape uniformity and narrow size distribution. At the same time, they are stable, non-toxic, conductive, and catalytically active. In the following section we will introduce main methods of AuNP preparation and explore how different fabrication procedures can result in different surface properties of nanoparticles.

2.1 Preparation of nanoparticles

Metallic nanoparticles have been used for centuries by artists and craftsmen during glass colouring processes. The first scientific report about synthesis and properties of colloidal gold, however, was not given until 1857 when Michael Faraday reported formation of a ruby red solution of colloidal gold [8]. Since then, numerous preparative methods have been made public, including both top-down and bottom-up approaches [9].

The top-down strategy resides in selective removal of a material from bulk, leaving only desired nanostructures, and common examples of such procedure are various lithographic techniques along with chemical etching. In the bottom-up method, atoms (emerging from reduction of ions in liquid) are assembled one by one under thermodynamic and chemical control, thus forming desired nanostructures. The major disadvantages of this approach are complicated control of monodispersity and necessity to overcome various thermodynamic barriers. Yet the possibility of large-scale production as well as the lowest dimension limit virtually being individual atoms outweighed those drawbacks and the overwhelming majority of colloidal nanoparticles is usually prepared by synthesis in aqueous solutions [10]. Moreover, thanks to an extensive recent research, various approaches to the nanoparticle synthesis are well explored nowadays.

The simplest and most common of these methods was developed by Turkevich et al. in 1951 [11]. It is based on chemical reduction of chloroauric acid ($HAuCl_4$) by sodium citrate, during which the reduced gold atoms slowly cluster together and are gradually being capped by the negative charge carrying citrate ions, which thus act as both reducing and stabilizing agent (see Figure 2.1). By careful adjustment of the reagents amount and reaction conditions it is possible to control the growth of nanoparticles. Further studies [12] enabled much precise and wider control over AuNP size and shape monodispersity, which has been essential in understanding of a relationship between their morphology and their optical response. They also

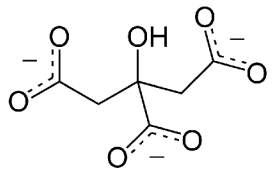

Fig. 2.1: Skeletal formula of a citrate ion, featuring three dissociated carboxyl groups, which play an important role in AuNP stabilization.

provided additional insight into kinetics of the reaction process [13, 14] as well as introduction of variety of other capping ligands such as thiols [15], polymers [16] or proteins [17].

Nowadays, it is possible to obtain very stable solutions with narrow distribution of nanoparticle sizes. On top of that, large scientifically driven demand made them commercially available from variety of suppliers (BBI, Ted Pella, Sigma-Aldrich), with diameters in the range of 2–250 nm, stabilized by various ligands or even pre-functionalized by proteins or polymer coatings, which is useful for further bioconjugation strategies (see Chapter 4).

The crystallographic structure of AuNPs is strongly dependent on a preparation procedure [18] and is usually quite complex rather than being perfectly monocrystalline [19]. Thanks to an extreme resolution provided by aberration-corrected transmission electron microscopy (TEM) and advances in 3D reconstruction algorithms a complete investigation of the inner structure, surface morphology, and even lattice strain at a single particle level is possible today. This is demonstrated by a TEM micrograph of a citrate capped nanoparticle on top of a graphene membrane in Figure 2.2. The columns of gold atoms forming a crystal lattice can be clearly seen as well as the weakly adsorbed citrate ions on the surface of the nanoparticle.

In the following section, the surface properties of metallic nanoparticles will be explained together with their relevance to ability of nanoparticles to self-assemble onto silicon surfaces.

2.2 Surface properties of nanoparticles

Nanoparticles used in this study bear a negative charge due to weakly adsorbed citrate ions. Unfortunately, it is not feasible to measure either charge or potential of the individual nanospheres in a colloidal solution. Therefore in colloidal science, the quantification is done by introducing so called zeta potential, which can be measured indirectly by various electrophoretic techniques [21]. The zeta potential is — in a simplified way — a value of electrostatic potential in some particular distance from

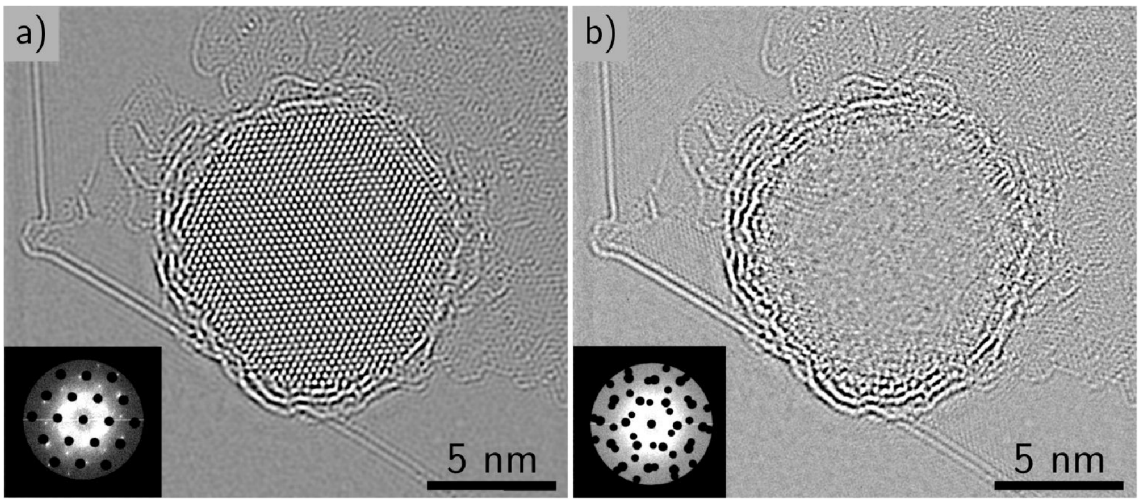

Fig. 2.2: An atomic resolution image of a 10 nm gold nanoparticle and its surrounding citrate capping agent on the top of a graphene membrane. **(a)** An enhanced-contrast filtered image, where the graphene reflections were subtracted in a digital diffractogram of the entire image (see inset). **(b)** An image of the citrate molecules, obtained by masking the graphene and gold reflections in the Fourier-transformed image in order to isolate and image the citrates. Adapted from [20].

a charged surface. Although it is in general very difficult to extrapolate the value of surface charge from the value of zeta potential, it has been shown that for some materials (including SiO_2) there is no difference between value of zero zeta potential and zero surface charge [22]. Therefore, it is in practice not necessary to distinguish e.g. between positively charged silicon surface and silicon surface with positive zeta potential.

The zeta potential of colloidal nanoparticles strongly depends on their surroundings. Because colloidal solutions are usually water-based, the concentration of both positive and negative ions becomes very important, as these ions are electrostatically attracted to a nanoparticle surface and gradually screen out its charge. For the stability of colloidal solutions it is crucial that individual nanoparticles repel each other and do not aggregate. Aggregation of nanoparticles might occur when the zeta potential decreases as a result of intense charge screening.

In Figure 2.3, the zeta potential of silicon dioxide, silver and gold nanoparticles in solutions having various pH is shown. It should be clear that thanks to the citrate capping (silver nanoparticles are made in a similar way to the gold ones) each nanoparticle bears a number of $-COO^-$ terminating groups, which may act as a sink for protons [27]. By definition, the concentration of protons increases with decreasing pH; therefore the zeta (surface) potential of nanoparticles also decreases with decreasing pH, which often leads to lower stability of solution and nanoparticle

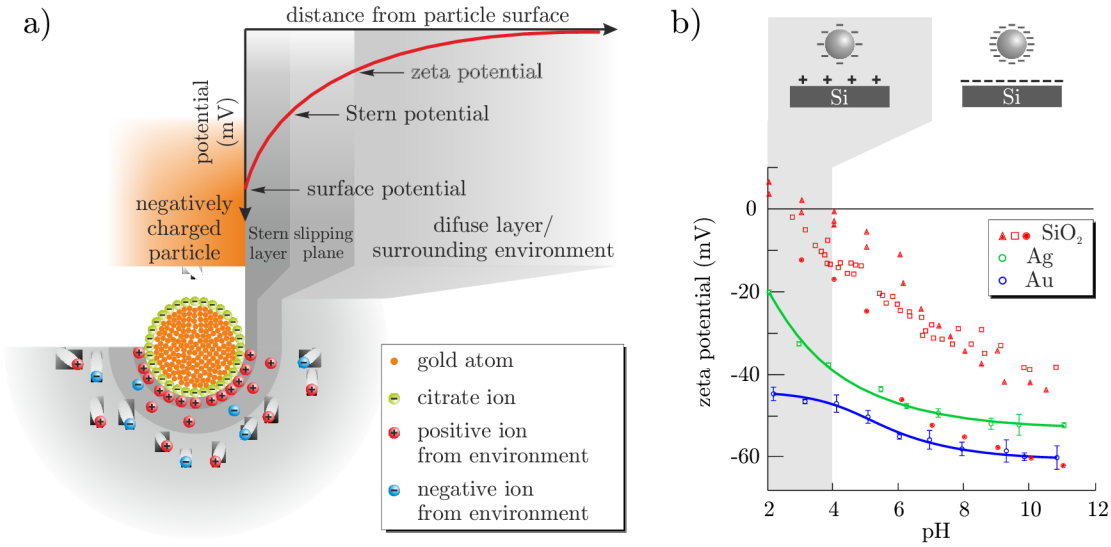

Fig. 2.3: a) Schematic illustration of colloidal gold nanoparticle surrounded by positive and negative ions from its environment. Relevant electrokinetic potentials [21], including zeta potential, are defined at interfaces between various layers. b) Zeta potentials of silica surfaces and gold/silver nanoparticles as functions of pH of the surrounding environment. Grey colour marks the region in which it is possible that silica/silicon surface and nanoparticles attract each other (see inset on top). The trend of the data for nanoparticles suggests the possibility of low stability of colloidal solution at low pH, namely silver nanoparticles being less stable than gold ones. Data adapted from [23, 24, 25] (SiO_2), and [26] (Ag/Au NPs).

flocculation in sufficiently acidic environment, i.e. aggregation of the nanoparticles due to lack of electrostatic repulsion at low pH and prevailing attractive van der Waals forces. Note, that colloidal solutions are usually considered unstable if their respective zeta potential value decreases below $\pm 30\,\mathrm{mV}$ [28].

In the case of silica surface it can be seen (Figure 2.3) that in the region around pH of 4 its zeta potential reaches zero (so called isoelectric point) and in more acidic environment it is even possible to measure positive zeta potential (corresponding to positively charged surface). Because the surface of a silicon wafer is under ambient atmospheric conditions always covered by a native oxide, one would expect that its behaviour should significantly resemble that of silica. This is partly true, but due to distinct final fabrication procedures the surfaces of silicon wafers may be terminated by different end groups ($-$H, $-$O$-$CH$_x$, $-$OH, ...). As a consequence, the isoelectric point will be different for silicon substrates with different fabrication history and the zeta potential curve will be shifted to more positive or negative values, depending on surface termination. The general shape of the curve (positive for low pH, negative for higher) will be preserved (see Section 2.3). The message

given in previous paragraphs and Figure 2.3 should be clear — there is a region of pH where colloidal nanoparticles and silicon surface may attract each other and the rate of their deposition on the surface could thus be efficiently increased. In the next section more profound description of this self-assembly process is provided together with an account of silicon wafers surface chemistry.

2.3 Self-assembly of gold nanoparticles onto solid substrates

In addition to application of free nanoparticles (biosensors [29], water treatment agents [30], or drug carriers [31]), there are many applications which require their immobilization and precise placement, such as enhancement of the efficiency of solar cells [3], selective growth of nanowires [4] or nanoparticle utilizaiton in the field of nanophotonics [5].

Silicon is a substrate of choice for deposition of nanoparticles as it is the leading platform for electronics integration and thus acts as a basis for linking conventional electronic circuits with plasmonic structures made of nanoparticles. The basic idea for nanoparticle deposition was indicated in the previous section: The typical colloidal gold solution has a pH of 5.5 whereas the isoelectric point of conventional silicon wafers varies between pH of 3–4 [32]. The adhesion of AuNPs to a silicon surface from the as-received solution is thus prevented by the repulsion between the two negatively charged surfaces, namely by $-COO^-$ termination of the gold colloidal nanoparticles and $-O^-$ termination of the native oxide on the silicon surface. To achieve self-assembly of AuNPs, the pH of their solution has to be lowered below the isoelectric point of a particular substrate, turning its surface potential to positive values [33], and consequently leading to enhanced deposition of AuNPs onto silicon surface.

Two silicon substrates of different origin have been used for experiments with the self-assembly of AuNPs. Although they are both covered with native oxide, their terminating chemical groups differ due to distinct final steps in corresponding silicon wafer fabrication. Silicon substrate denoted in further text as sample A have been dried in hot isopropyl alcohol as the last step of the fabrication. Because of that, the surface of its native oxide is terminated by $-H$ and $-CH_x$ surface groups which give rise to its hydrophobic behaviour [34]. Sample B, on the other hand, have been rinsed in ultraclean water at the end of a fabrication process, and its native oxide is terminated by hydrophilic $-OH$ groups [7]. The properties of both types of samples are summarized in Table 2.1.

Tab. 2.1: An overview of important properties of two distinct types of silicon wafers used in the experiments with AuNPs self-assembly. Notation of less or more hydrophilic surface is based on contact angle measurements in Ref. [7].

	Sample A	Sample B
Manufacturer	Siltronix	ON Semiconductor
Orientation	111	100
Resistivity ($\Omega\,$cm)	0.01	6–9
Final bath	isopropyl alcohol	ultraclean water
Termination	$-$H, $-$CH$_x$, $-$OH	$-$OH
Surface	more hydrophobic	less hydrophobic

As indicated in Section 2.2, the surface groups strongly affect the value of isoelectric point of the substrate because they are susceptible to protonation or deprotonation i.e. addition or removal of protons from their molecules. The degree of (de)protonation at given pH is characterized by a dissociation constant, which varies for different surface groups. Consequently, the overall surface potential involves contributions of all charged species which have arisen on the surface due to (de)protonation.

The difference in isoelectric points of the two substrates was confirmed by experiments on deposition of AuNPs (BBI, which are summarized in Figure 2.4. Since the isoelectric point of the sample B is lower than the pH of as-received colloidal solution (pH 5.5), the deposition of nanoparticles is blocked by electrostatic repulsion. Acidification of the solution to the pH of 4, however, turns the surface potential of the sample B to positive values and the deposition rate of AuNPs is significantly increased (compare insets I and II in Figure 2.4). Although such pH is sufficient for deposition onto a sample B, the deposition is still prevented onto a sample A (see inset III in Figure 2.4). Therefore even more acid has to be added to shift the solution pH to the value of 2.5. Only then the polarity of the surface potential is reversed and the deposition is enabled (inset IV in Figure 2.4). The reason for this behaviour is the difference in surface groups of respective silicon wafers. Sample A is initially more resistant to oxide etching due to $-$H and $-$CH$_x$ surface termination [35] so higher concentration of acid has to be used for colloidal solution modification. In sufficiently acidic solution, the oxide is being etched and oxidized at the same time. This results in exchange of surface groups which are now replaced by hydrophilic $-$OH groups [34]. The sample surface potential is turned positive (at lower pH though) and the deposition proceeds in the same way as for sample B. It should be noted that despite the crystallographic orientation and resistivity is different for sample A

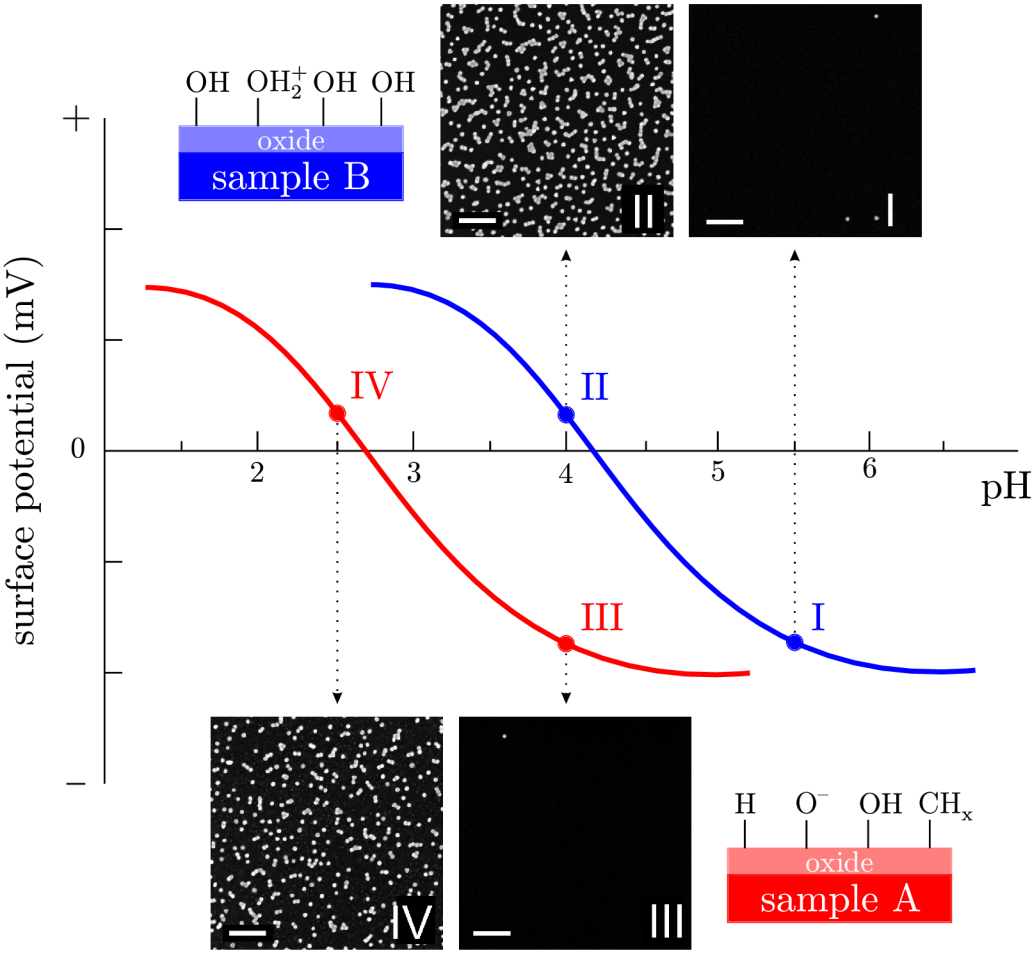

Fig. 2.4: Schematic representation of the surface potentials of silicon wafers with two different isoelectric points. The insets are SEM micrographs of sample surface after 2 h immersion in colloidal solutions of AuNPs (diameter 20 nm) with modified pH. Insets I and II show sample B after immersion in an as-received and 3 mM HF-modified solution, respectively. Insets III and IV show sample A after immersion in 3 mM and 12 mM HF-modified solution, respectively. Scale bars are 200 nm. After [7].

and sample B (see Table 2.1), experiments have shown that none of these factors matters in the self-assembly of AuNPs [7].

2.4 Guided assembly of nanoparticles

Optical properties of metallic nanostructures will be fully described in Chapter 3 but we will mention now that they strongly depend on their size and geometry. Ensembles and clusters of metallic and core-shell metal-dielectric nanoparticles may act as building blocks of various nanostructures. Examples of such application cover plasmonic waveguides [36], nanostructures for second harmonic generation [37], or tuneable plasmonic antennas that support a broad range of resonances (see Figure 3.4 in Chapter 3).The precise control over spatial organization of nanoparticles, their interparticle distances and mutual orientations is therefore required.

Under normal conditions nanoparticles adhere to a substrate surface randomly. For reasons explained in the previous paragraph it is of great interest to control their spatial distribution.Vast majority of approaches developed so far can be classified within three categories where the control of assembly process is based on chemical recognition, electrostatic attraction, or surface topography patterning.

For the chemically driven self-assembly the key factor is binding of nanoparticle capping molecules to patterns made of counterpart molecules. Such molecular-based positioning typically employs templates (made of thiolated DNA [38] or alkanethiols) which are fabricated using photolithography, electron beam lithography (EBL), micro-contact printing, or dip-pen nanolithography [41] (Figure 2.5a). In one example of such "chemical EBL", molecular patterns were formed by electron irradiation via selective conversion of terminal groups of large molecules self-assembled on the silicon surface, whose protonated states then served as binding sites for nanoparticles covered with the negative citrate [42]. Self-assembly guided by electrostatic attraction is usually achieved by charging of an insulating layer (e.g. polymer) using electron beam [43, 44] or by trapping the charge inside so called electret layer [45, 39] (Figure 2.5b). Another approach to the controlled assembly of nanostructures which is based on controlling the surface topography by means of EBL (e.g. assembly of polystyrene latex particles [46]) and/or utilization of capillary forces, which can overcome thermal fluctuation and guide the assembly of particles during their solvent evaporation (e.g. AuNPs [47]) — see Figure 2.5c.

Although strategies described in previous paragraphs have proven themselves to be useful for guiding the self-assembly of particles with dimensions on both micro- and nanometer scale, they indeed have some drawbacks: Large amount of steps sometimes makes the whole fabrication procedure rather complex, patterned substrate can change the optical response of nanostructures [40], and interfacial layers are undesirable for some applications, e.g. because they interfere with plasmon resonance of metallic nanoparticles. Even the mono-molecular layer employed in Ref. [42] can alter the performance of e.g. sensing devices.

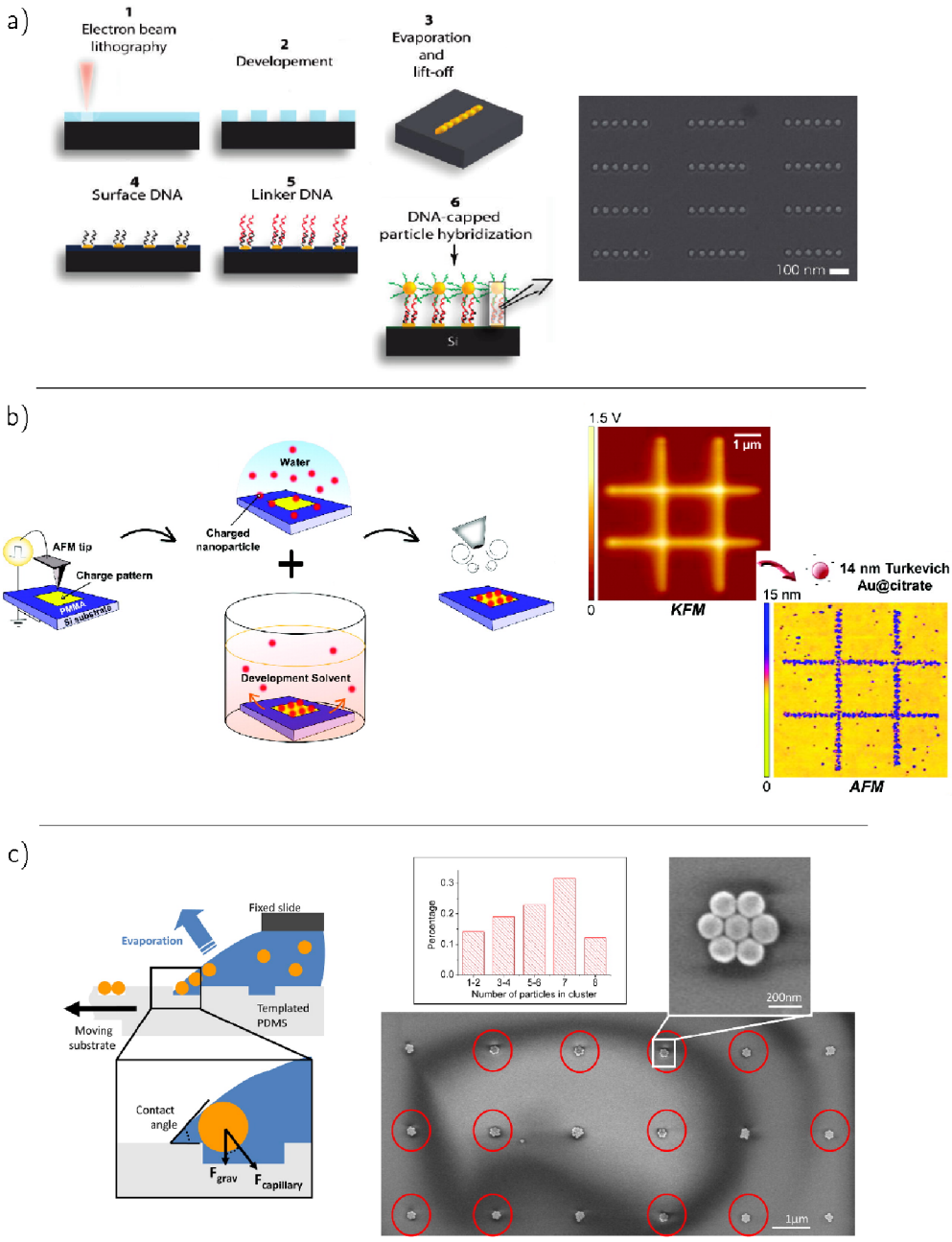

Fig. 2.5: Three types of directed self-assembly. **(a)** Chemical recognition: Fabrication of nanopatterns by EBL is followed by their functionalization with thiol-terminated DNA and subsequent hybridization with DNA-capped AuNPs. After [38]. **(b)** Electrostatic attraction: Charge is "written" into a 100 nm PMMA thin film by an AFM tip. Then the sample is immersed in a gold colloidal solution and developed in an adequate solvent. After [39]. **(c)** Topography-based assembly: Water droplet containing silica-gold nanoshells is sandwiched between glass slide and substrate with an EBL-patterned polymer layer. By moving the droplet meniscus across the substrate the particles are pushed into the voids by capillary forces. This results in an assembly of heptamers on the template with 32% yield. After [40].

These problems have been overcome by our group as we have achieved guided self-assembly of AuNPs onto bare silicon substrate pre-patterned by ion or electron beams [7]. Our previous work was mostly focused on Ga^+ ions. Due to lower sample damage, and also smaller probe size, in this work we have concentrated on electron beams. The crucial element of this procedure — the modification of sample surface by impinging electrons or ions — will be described below, together with experimental results showing structures fabricated this way.

2.5 Patterning of silicon substrates by electron beam

For fabrication of ensembles made of precisely placed nanoparticles a novel approach developed by our group was used. The fundamental advantage of this approach is an exclusion of any additional interlayer or topography template — only bare silicon surface irradiated by electron or ion beam serves as a template for guided deposition of AuNPs from colloidal solution. The control over deposition is attained by appropriate electron fluence (number of electrons per unit surface, cm^{-2}) during the irradiation step together with a pH-modification of the solution during the assembly step.

Two modes of patterning procedure can be distinguished on samples exposed to different fluences of electrons. Exposure to an electron beam with low fluence promotes exchange of significant surface groups: On sample A, $-H$ and $-CH_x$ groups are most likely to be replaced by $-OH$ groups (under normal atmospheric conditions); on sample B the number of $-OH$ groups, which are already present on that type of sample, is increased. As these groups are susceptible to protonation in acidic environments ($-OH \rightarrow -OH_2^+$), on both samples this leads to stronger affinity of nanoparticles towards their surface compared to non-irradiated sites. Exposure to higher fluences of electrons, on the other hand, limits the adsorption of nanoparticles and eventually blocks it completely. This outcome can be attributed to a contamination layer produced by beam-induced decomposition and subsequent deposition of hydro- and fluorocarbons adsorbed on the surface prior to irradiation [48]. Evidences supporting this conclusion were provided by XPS and FTIR spectrometry [7].

It has been already described in Section 2.3 that pristine surface of sample A does not attract nanoparticles unless their colloidal solution is substantially acidified. Yet after exposure to proper fluence of electrons the surface groups are modified and adsorption of nanoparticles upon the exposed area is promoted. Examples of sample A patterned by electron beam are shown in Figure 2.6. It can be clearly seen how the increasing fluence of electrons promotes nanoparticle adhesion. When

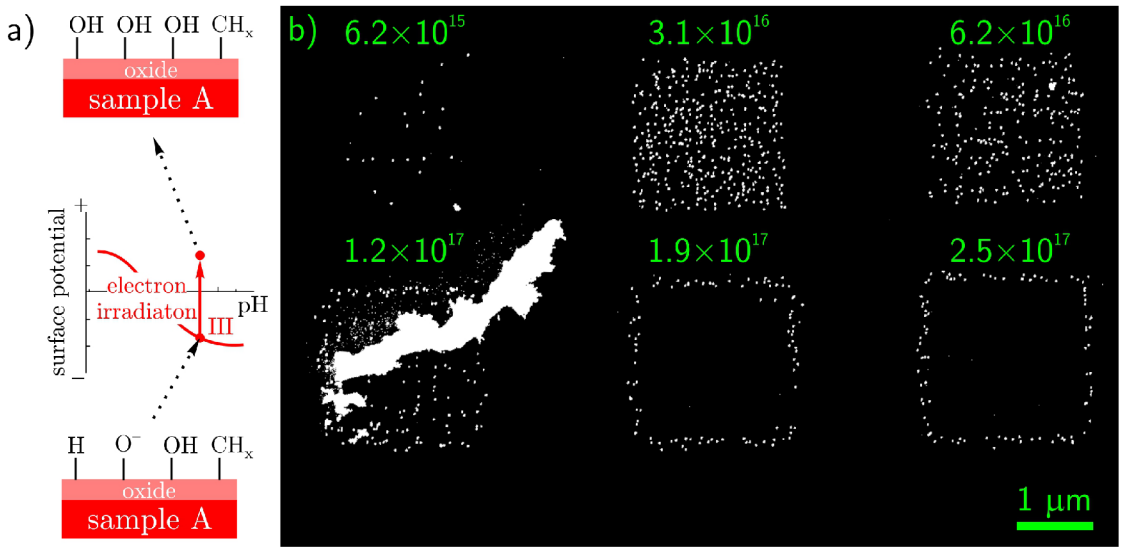

Fig. 2.6: Deposition of AuNPs on sample A with square patterns exposed to electron beam. **(a)** Schematic illustration of low fluence electron irradiation impact on surface terminating groups and surface potential of sample A .**(b)** SEM micrograph of sample A surface, pre-patterned by 5 keV electrons, after 2 h immersion in the colloidal solution of AuNPs with mean diameter 20 nm modified by 2.5 mM hydrofluoric acid. The $2\times2\,\mu m^2$ squares were irradiated with fluences (cm^{-2}) inscribed above each of them. The large white spot is a piece of dust contaminating the sample.

an optimal fluence is used, a dense layer of nanoparticles covers the exposed area (positive deposition). Its further increase, however, gives rise to contamination of the surface and the deposition of nanoparticles from solution is suppressed in the end. The rim of nanoparticles adhered around the overexposed area is due to its irradiation by a Gaussian tail of the electron beam [48].

Analogous procedure can be performed on the sample B, as demonstrated in Figure 2.7. Opposed to the sample A, an unexposed surface of this sample attracts nanoparticles from slightly acidified solution so the starting concentration of nanoparticles on the surface is already high. Nevertheless, there is still an increase in their amount on areas exposed to low fluences of electrons. For higher fluences, the contamination again takes place and nanoparticles cover only areas which have not been irradiated by the electron beam (negative deposition). Unfortunately, the rim caused by inhomogeneous beam intensity profile can be observed again.

To demonstrate the fabrication potential of negative deposition, squares and circles with various dimensions were patterned on the surface of sample B with high fluence of electrons. The result is shown in Figure 2.8, where one can clearly see that with this approach it is possible to control the assembly of nanoparticles down to the sizes of 1 µm. Below this scale, the effects of beam shape and scanning path become

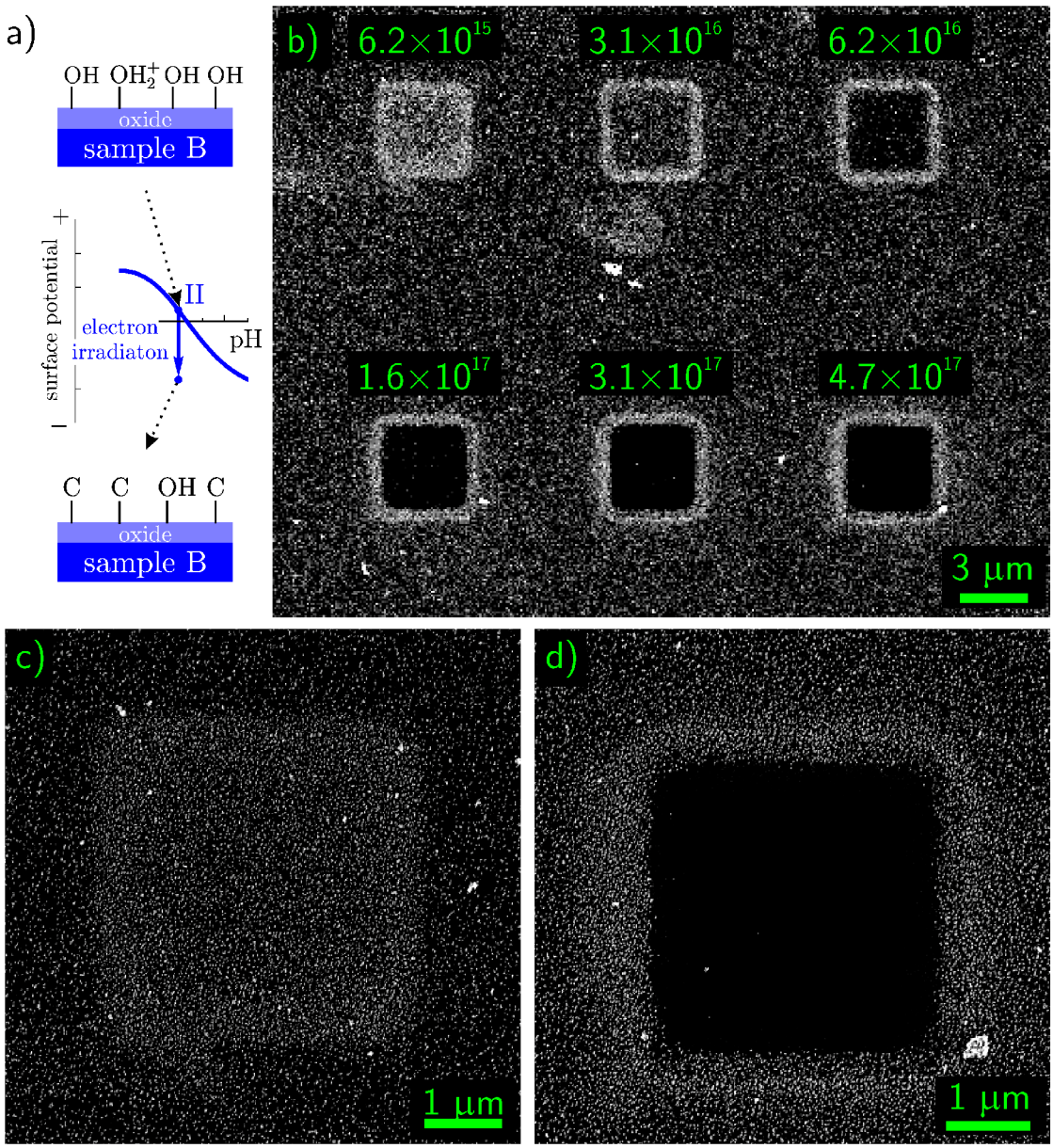

Fig. 2.7: Deposition of AuNPs on sample B with square patterns exposed to electron beam. **(a)** Schematic illustration of electron irradiation impact on surface terminating groups and surface potential of sample B. **(b)** SEM micrograph of sample B surface, pre-patterned by 5 keV electrons, after 2 h immersion in the colloidal solution of AuNPs with mean diameter 20 nm modified by 2.5 mM hydrofluoric acid. The $3{\times}3\,\mu m^2$ squares were irradiated with fluences (cm^{-2}) inscribed above each of them. Below are magnified images of squares patterned with **(c)** lowest fluence ($6.2 \times 10^{15}\,cm^{-2}$) and **(d)** highest fluence ($4.7 \times 10^{17}\,cm^{-2}$), respectively. Please note that due to low magnification of the images, the individual AuNPs might not be resolved, but their presence is indicated by brighter areas.

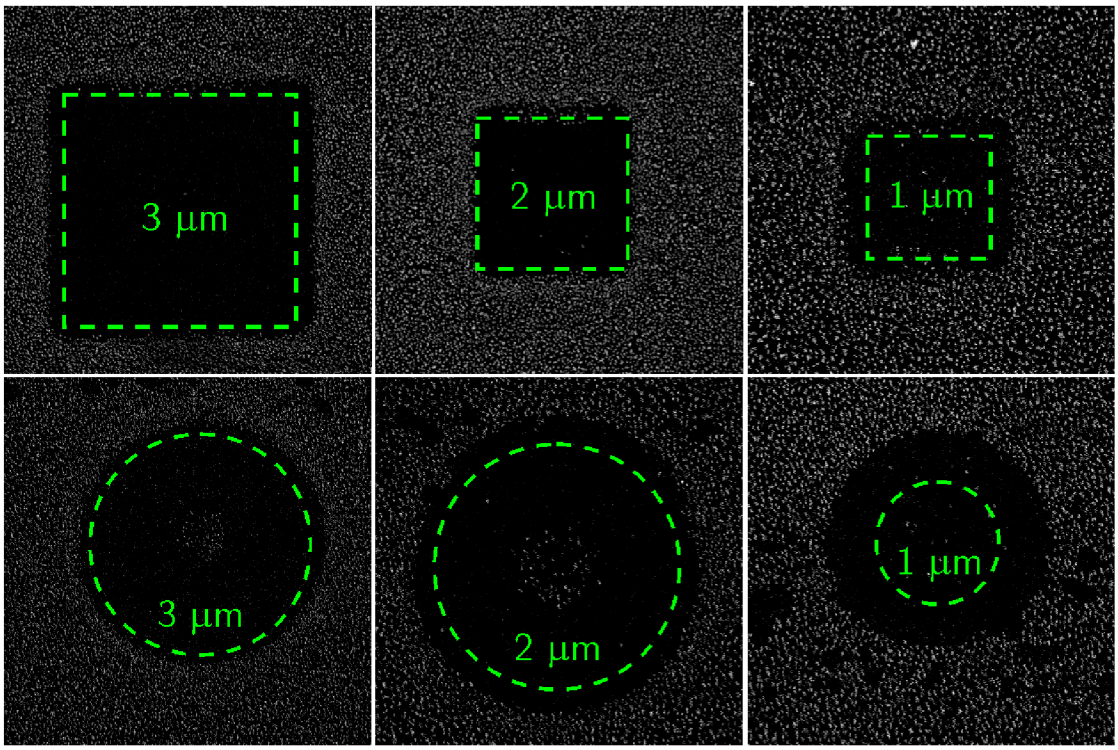

Fig. 2.8: Examples of negative deposition. Images are SEM micrographs of squares and circles patterned by 5 keV electrons on sample B, which was then immersed for 2 h in a colloidal solution of AuNPs with mean diameter 20 nm modified by 2.5 mM hydrofluoric acid. The shapes and sizes of irradiated areas are marked by dashed lines with relevant side or diameter dimensions inscribed. The fluence of electrons was $4.4 \times 10^{17}\,\mathrm{cm}^{-2}$ for all shapes. Please note that view fields are not the same for all images in order to show a reasonable amount of details.

more significant. Notice, for example, the groups of nanoparticles in the centres of patterned circles, which are remnants of spiral scanning path of electron beam, or how nanoparticles are pushed away from the intended irradiation area. The control over resulting structure is therefore limited in these cases.

One possible way how to overcome some of the problems described above is to use negative deposition to produce positive-like structures (pseudo-positive deposition). The resultant structures then resemble those fabricated by positive deposition on a small scale but on a large scale it is clear they were fabricated using negative-type deposition. Examples of such structures are shown in Figure 2.9. It can be seen that resultant squares and circles consist of nanoparticles which were repelled from the irradiated annular area. The size of fabricated structures is thus reduced while maintaining a good quality of their outline. But still, the precise positioning of individual nanoparticles is difficult to achieve using this method.

The most suitable approach to accurate nanoparticle arrangement seems to be

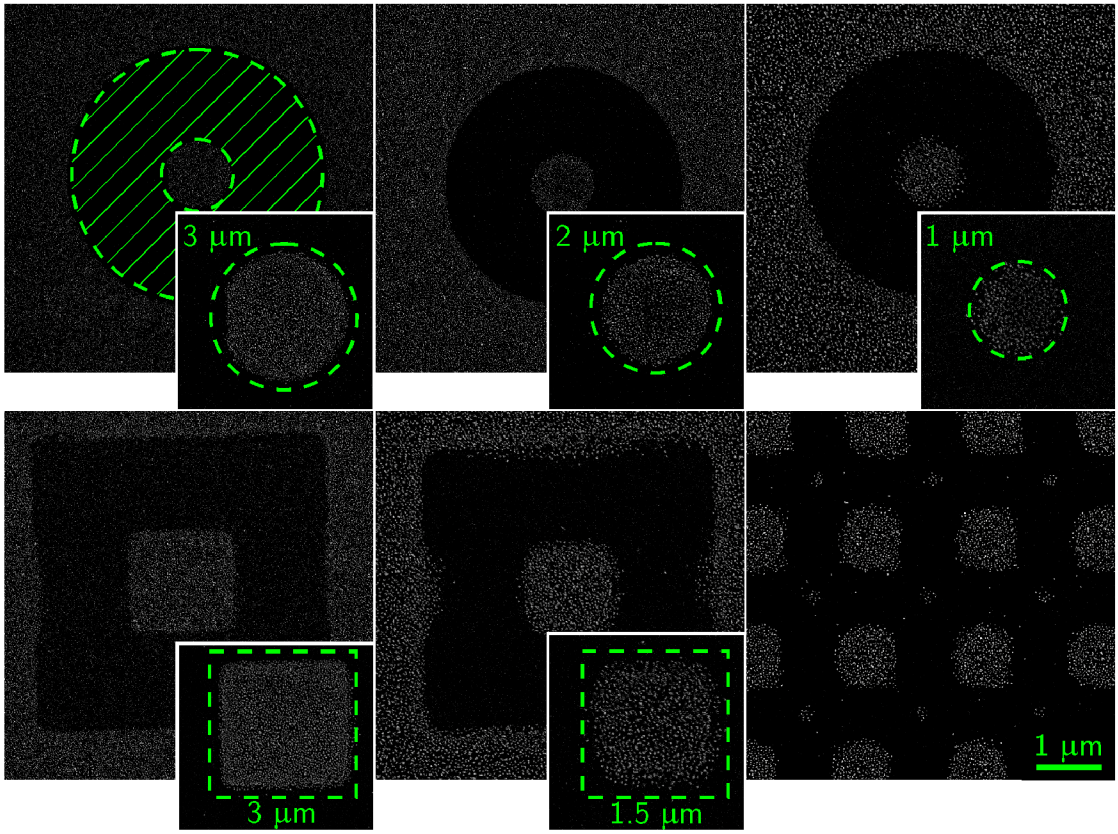

Fig. 2.9: Examples of pseudo-positive deposition of AuNPs. The patterns on the surface of sample B were irradiated by 5 keV electrons with fluence of $4.4 \times 10^{17}\,\mathrm{cm}^{-2}$ and immersed for 2 h in a colloidal solution of AuNPs with mean diameter 20 nm modified by 2.5 mM hydrofluoric acid. Exposing annular areas (one example hatched) to electron beam results in structures (detailed on insets) which resemble those achieved by positive deposition.

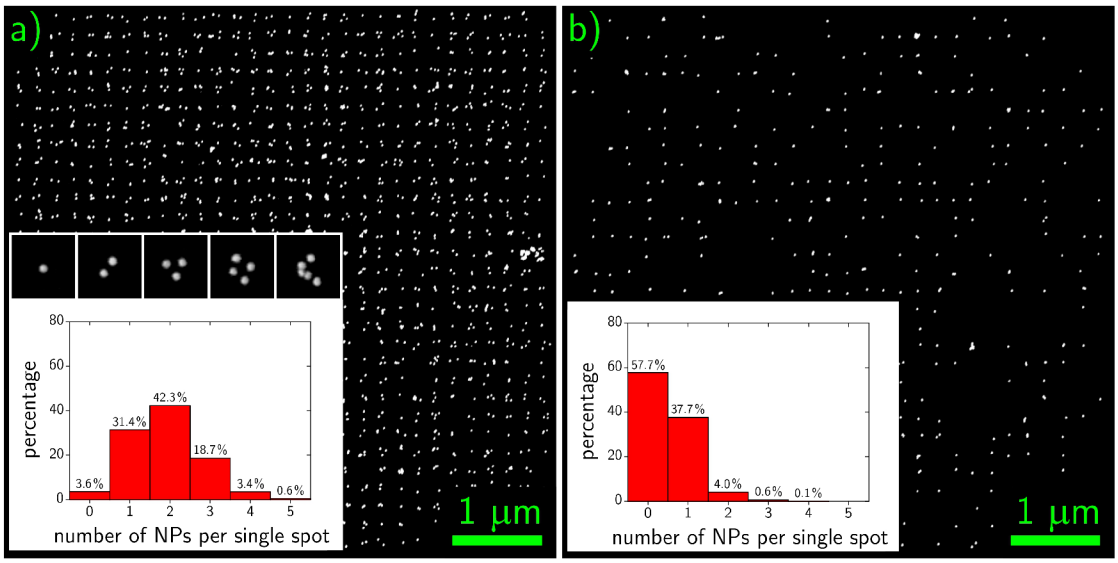

Fig. 2.10: The role of irradiated spot dimensions in positive depositions. SEM images show the surface of sample A, patterned by 5 keV electrons and immersed for 2 h in a colloidal solution of AuNPs with mean diameter 20 nm modified by 2.5 mM hydrofluoric acid. The fluence of electrons ($2.3 \times 10^{16}\,\mathrm{cm}^{-2}$) and the pitch of rectangular grid of irradiated spots (200 nm) were equal in both cases; the diameter of circular spots was different though, being 100 nm in a) and 20 nm in b). Bar graphs in both images show a percentage at which a particular number of AuNPs can be found at the irradiated spots (see examples of 20 nm AuNP clusters in a).

the positive deposition. In Figure 2.10 it is shown how by reducing the size of irradiated spots we can achieve guided assembly into clusters consisting of only several nanoparticles. Insets show the percentage at which particular number of nanoparticles can be found at individual irradiated spots. In the left image, the number of nanoparticles at each spot is most likely between 1–3 for irradiated circular spots with diameter of 100 nm. With decreasing diameter a lot of vacant places appear. This is depicted in the right image, where unoccupied sites dominate the statistics of irradiated 20 nm spots.

Similar impact on the quality of resultant assembled clusters has the change in fluence of electrons as highlighted in Figure 2.11. Low fluences are insufficient to promote adsorption of nanoparticles and significant amount of vacant spaces is present in the patterned grid. As the fluence increases, the histogram maximum shifts and for sufficiently high fluences two-and-more clusters become prevalent.

In this chapter it has been shown that by applying the knowledge of surface chemistry of both colloidal nanoparticles and solid substrates it is possible to control nanoparticle self-assembly with very good reliability. Although only the case of 20 nm AuNPs and silicon has been manifested, the method was also successfully

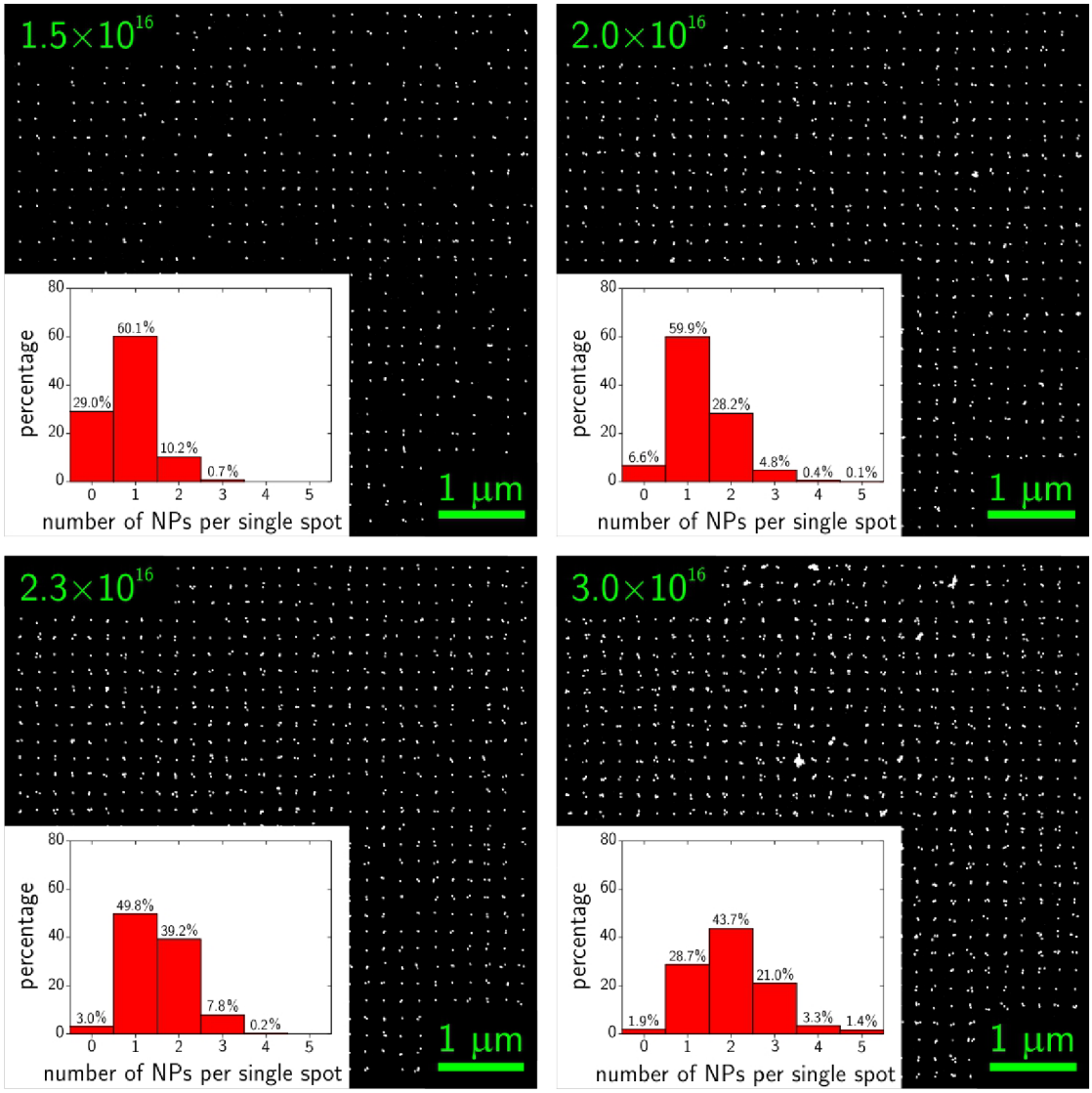

Fig. 2.11: The role of electron fluence in positive depositions. SEM images show the surface of sample A, patterned by 5 keV electrons and immersed for 2 h in a colloidal solution of AuNPs with mean diameter 20 nm modified by 2.5 mM hydrofluoric acid. The pitch (200 nm) of a rectangular grid and diameter of irradiated spots (60 nm) was the same for all patterns; the fluence of electrons (cm^{-2}) is different in each image and it is inscribed in top-left corners. Insets show a percentage at which a particular number of AuNPs can be found at irradiated spots.

applied to AuNPs with larger and smaller dimensions. The general scheme is most likely applicable also to other materials (e.g. silver nanoparticles). Moreover, using charged particle beams it is even possible to pattern the substrate and thus achieve a guided self-assembly of nanoparticles onto previously selected areas. With correct spot-size and electron fluence one can carry out nanoparticle deposition with almost single particle precision. The shape of irradiated spot has proven to play a significant role as well (results have not been shown) which is introducing an idea of patterning the surface by spots of various shapes which would then facilitate the assembly of only specific clusters or short chains of nanoparticles. With such ensembles of nanoparticles special optical properties are often associated [40], and even the nanoparticles themselves response to electromagnetic radiation in a way which is different from bulk. These properties will be addressed comprehensively in the following chapter.

3 OPTICAL PROPERTIES OF METALLIC NANOSTRUCTURES

Metallic nanoparticles have been studied mainly because of their size- and shape-dependent optical and electronic properties, which can be illustrated on example of bright colours of noble metal colloidal solutions. This phenomenon is a direct consequence of resonantly enhanced absorption and scattering of light in the visible range of electromagnetic spectrum. The enhancement is based on collective oscillations of free conductive electrons coupled to an interacting electromagnetic field (so called surface plasmon polaritons, SPP, or simply surface plasmons).

In the case of metallic nanostructures, whose conduction electrons are confined within the nanostructure itself, a non-propagating form of the resonant conduction electron excitation takes place — so called localised surface plasmon resonance (LSPR). In the following paragraphs it will be shown how LSPR arise naturally from the electrodynamics of conductive particles in an oscillating electromagnetic field, and what consequences it has for their optical properties.

3.1 Theory of scattering by small particles

The problem of scattering and absorption of electromagnetic radiation by a sphere was originally solved by Mie in 1908 using Maxwell's equations [49]. Yet for qualitative analysis his full multipole solution is not necessary, and the lowest-order approximation (so called quasi-static or dipole approximation) can be used instead. Note, however, that this approximation is valid only for nanoparticles with dimensions much smaller than wavelength of the incident light. As long as this condition is fulfilled, the retardation effects (i.e. phase shifts of the electromagnetic field over the nanoparticle diameter) are negligible, and it is sufficient to take into account only dipolar oscillations.

As illustrated in Figure 3.1, the electric field of an incoming light induces polarization of free conduction electrons across the particle. Much heavier ionic cores then give rise to a restoring force which causes electron oscillations. Nanoparticles illuminated by light thus act in a way analogous to radiating dipoles. The dipole moment $\mathbf{p}$ induced inside a homogeneous, isotropic sphere of radius R located in uniform electrostatic field $\mathbf{E}$ is given by

$$\mathbf{p} = 4\pi\varepsilon_0\varepsilon_\mathrm{m}R^3\frac{\varepsilon-\varepsilon_\mathrm{m}}{\varepsilon+2\varepsilon_\mathrm{m}}\mathbf{E}, \tag{3.1}$$

where ε and ε_m are dielectric functions of the sphere and surrounding medium, respectively; both being complex functions of the frequency of light [50].

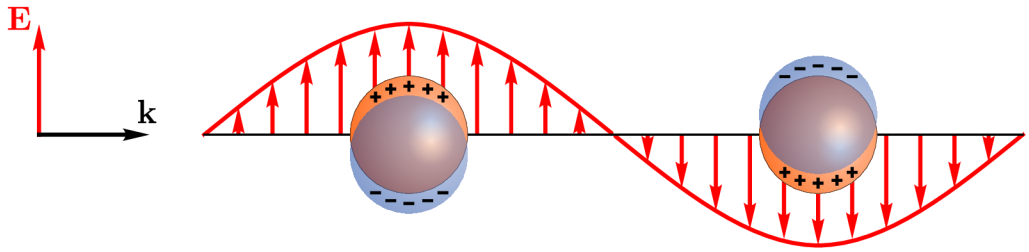

Fig. 3.1: Schematic illustration of metallic particles illuminated by an electromagnetic wave with wavevector **k**. Electric field **E** forces electron "cloud" to move, whereas much heavier ionic cores are virtually unaffected. When the size of particle is much smaller than the wavelength of light it is reasonable to consider the field homogeneous on the scale of particle dimensions.

The polarizability α, defined via $\mathbf{p} = \varepsilon_0 \varepsilon_\mathrm{m} \alpha \mathbf{E}$, is therefore

$$\alpha = 4\pi R^3 \frac{\varepsilon - \varepsilon_\mathrm{m}}{\varepsilon + 2\varepsilon_\mathrm{m}}. \tag{3.2}$$

It follows from (3.2) that polarizability goes through a resonance under a condition that $|\varepsilon + 2\varepsilon_\mathrm{m}|$ is minimal. Hence it is the relation between dielectric constants of sphere and surrounding medium (which are both functions of wavelength) that influences the resonant wavelength and shape of a plasmon resonance peak. For silver and gold, this condition is met in the visible part of the spectrum, whereas for other metals its in the near-infrared and the resulting peaks are much broader. This resonance is also the reason for enhancement of both near fields and efficiency with which metallic nanoparticles scatter and absorb light. Useful quantities that characterize this phenomenon are corresponding cross sections C_sca and C_abs [51]:

$$C_\mathrm{sca} = \frac{k^4}{6\pi} |\alpha|^2 = \frac{8\pi}{3} k^4 R^6 \left| \frac{\varepsilon - \varepsilon_\mathrm{m}}{\varepsilon + 2\varepsilon_\mathrm{m}} \right|^2 \tag{3.3a}$$

$$C_\mathrm{abs} = k \mathrm{Im}\left[\alpha\right] = 4\pi k a^3 \mathrm{Im}\left[\frac{\varepsilon - \varepsilon_\mathrm{m}}{\varepsilon + 2\varepsilon_\mathrm{m}} \right], \tag{3.3b}$$

with wavenumber $k = 2\pi/\lambda$. Expressions (3.3) reveal that scattering and absorption efficiencies strongly depend on particle dimensions, and how they are both enhanced when the condition for plasmon resonance is met. It is worth noting that these cross sections characterize transverse electromagnetic waves far away from the particle. The electric near field in its vicinity must be normal to the surface in order to satisfy the boundary conditions. Therefore the outgoing waves in the near-field region of a particle differ from those in the far field, which is fundamental for some applications — e.g. surface-enhanced Raman spectroscopy (SERS) [52, 53] or the electromagnetic coupling of nearby nanoparticles (see Section 3.3).

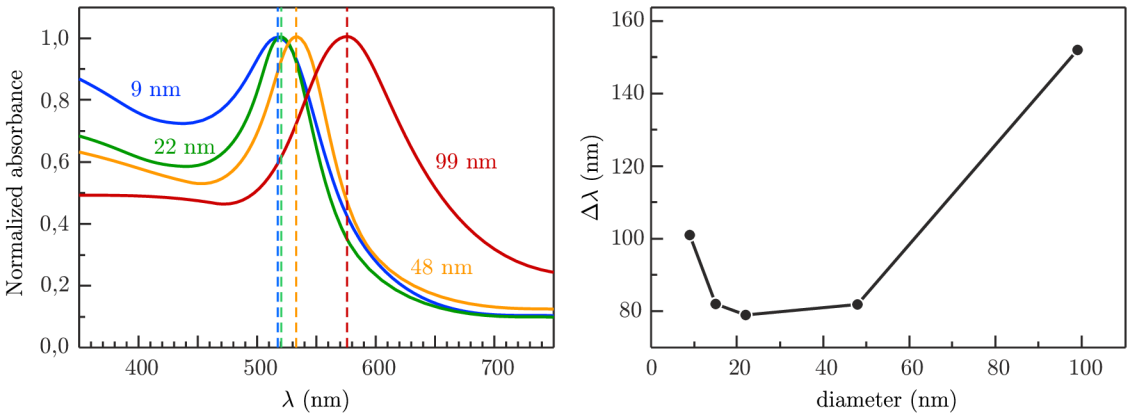

Fig. 3.2: (Left) Absorption spectra of colloidal solutions of spherical AuNPs with various diameters. All spectra are normalized at their absorption maxima, which are 517, 521, 533, and 575 nm, respectively. **(Right)** The plasmon bandwidth $\Delta\lambda$ as a function of particle diameter. After [54].

3.2 Limitations of Mie's theory

The results of quasi-static approximation provide basic insight into mechanisms behind LSPR of small metallic nanoparticles. For nanoparticles with dimensions comparable to the wavelength of visible light, however, this approach is no longer valid. As the size of nanoparticles increases, higher-order modes begin to play a major role because incident electromagnetic waves can no longer polarize the nanoparticles homogeneously. This retardation effect results in broadening of the plasmon resonance peak in the spectra and, as these higher modes peak at lower energies, also in its red shift with increasing particle size. This so called extrinsic size effect is illustrated in Figure 3.2.

Another important aspect is also evident in the Figure 3.2. For metallic nanoparticles with dimensions below 10 nm the plasmon bandwidth $\Delta\lambda$ anomalously increases. In the quasi-static limit of Mie's theory the size dependence of the position and bandwidth of plasmon resonance can not arise from electrodynamics (only scattering intensity depends on particle volume, see Equation 3.3). Hence another effect must give rise to it and to explain this behaviour we must address the dielectric function of particle, which is incorporated into the theory as an input parameter. If size of particle is large, $\varepsilon(\omega)$ of appropriate bulk material can be inserted into the Mie's equations, which then describe the optical properties correctly. For small nanoparticles though, so called intrinsic effects come into play and we usually incorporate them into the theory using size-dependent dielectric functions $\varepsilon(\omega, R)$ [55]. Intrinsic size effects reflect both changes in the structure of material as well as the influence of the particle surface on the electronic structure and charge densities, which are

both not covered by bulk dielectric function. The applicability of bulk dielectric functions for nanoparticles with small dimensions is discussed e.g. in Ref. [56].

To summarize, the theoretical approach of Mie provides us with useful insight into optical properties of small metallic particles. One should be careful though, about the limits of the theory. For large nanoparticles, full multipole solution must be taken into account; for small nanoparticles, the bulk dielectric function cannot be used any more and other effects must be incorporated into the theory. Nanoparticles which were used in this work are situated somewhere between these two limits. On the lower boundary, AuNPs with diameter of 20 nm are often successfully described with bulk gold optical properties, but for smaller nanoparticles this might be questionable. On the upper boundary, the 80 nm AuNPs reach almost one quarter of the visible light wavelengths and the assumption of homogeneous field is rather disputable too.

It should be also pointed out that an analytical solution of optical properties related to surface plasmon is available only for spheres and spheroids [57] and we must use numerical methods for solving Maxwell's equations in other geometries. These include discrete dipole approximation (DDA) [58], finite-difference time-domain (FDTD) [59] or finite element methods (FEM) [60], where the nanostructure of interest is represented as a number of finite polarizable elements whose mutual interactions with applied electric field are calculated in frequency or time domain. The results are typically well consistent with experiment [61].

Development of these methods together with increased computational power available paved the way for large number of studies describing dependence of plasmon resonance spectra on different shapes of nanoparticles, including triangular prisms, disks, wires, cubes, etc. [62]. An example of unique optical properties arising from non-spherical shape of nanoparticles is shown by extinction spectra of gold nanorods in Figure 3.3. Gold nanorods possess a weak transverse band in the visible region corresponding to electron oscillations along the short axis (similar to gold nanospheres), but also a strong longitudinal band in the near-infrared region corresponding to oscillations along the long axis. The latter resonance is very sensitive to the structure of nanorods and experiences a red-shift with increasing aspect ratio. When comparing this red-shift to that of spherical nanoparticles with various diameters (Figure 3.2), it is obvious that much smaller size variation (in aspect ratio) is sufficient for even larger shift of a plasmon resonance peak. This reveals how understanding the mechanisms of anisotropic growth of nanoparticles can result in precise control of the resonance conditions with the possibility to shift it through a region spanning several hundreds of nanometers.

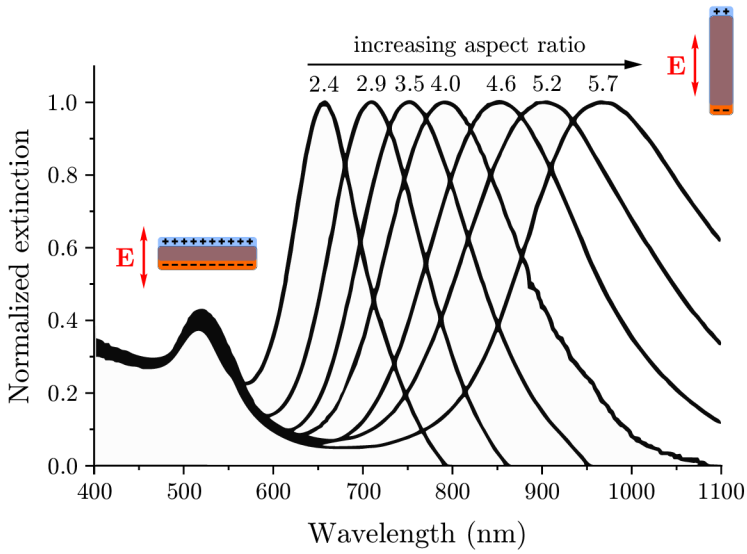

Fig. 3.3: Tuning of aspect ratios of gold nanorods results in different extinction spectra. Qualitatively, extinction is amount of light taken away from the light beam passing through solution of nanoparticles, and it consists of both scattering and absorption contributions [51]. Two modes of electron oscillations driven by electric field **E** (schematically shown) result in two modes of surface plasmon resonance — weak transverse mode insensitive to shape of nanorods and strong longitudinal mode experiencing large red-shift with increasing aspect ratio of gold nanorods. After [63].

3.3 Optical properties of nanoparticle ensembles

Another limitation of Mie's theory is an assumption of individual non-interacting particles. This is reasonable approximation when the density of nanoparticles in 3D or 2D is low. However, when aggregates of metallic nanoparticles are formed either spontaneously in liquid or intentionally by guided assembly, the electric field around the particle at plasmon resonance affects the surrounding particles and the optical response of the whole ensemble is changed. In other words, to appropriately model an optical response of dense layers and aggregated clusters of metallic nanoparticles, apart from material properties and geometrical shapes, which characterize isolated nanoparticles, an explicit knowledge of the statistical variation of the positions and pairwise distances of all particles should be taken into consideration [64].

The optical response of small clusters of nanoparticles can be calculated by means of the same numerical methods mentioned above (DDA, FDTD, FEM) as well as surface integral approaches including boundary element method (BEM) [65]. It should be noted though that as nanoparticles almost touch each other in these clusters, coupling to higher order modes such as quadrupole resonance becomes more and more important, and methods which do not take these into account become con-

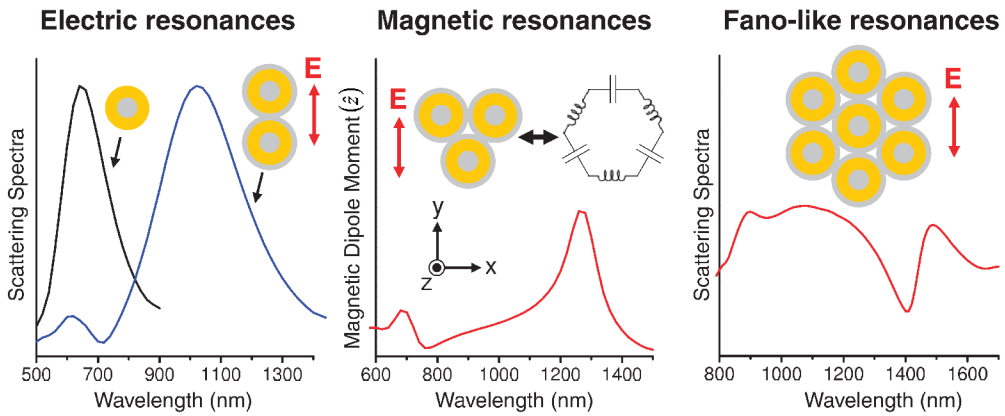

Fig. 3.4: Self-assembled nanoshell clusters can be tailored to support tuneable electric, magnetic, and Fano-like resonances. Electric dipole resonances generally exist for all plasmonic nanostructures and are shown here for individual nanoshells and coupled dimers (left). Packed trimer clusters exhibit magnetic dipole resonances and can be described as a closed loop of nanoinductors and nanocapacitors (middle). Fano-like resonances are supported by heptamers (right). These simulations use nanoshells with inner and outer radii of the gold shell $[r_1, r_2] = [62.5, 85]$ nm. The clusters have 2 nm wide gaps filled with dielectric spacer (dielectric constant $\varepsilon = 2.5$). Adapted from [67].

siderably inaccurate [66]. Examples of optical properties of clusters constituted by silica-gold nanoshells (calculated using FEM, Comsol) are shown in Figure 3.4. The strong electric, magnetic, and Fano-like resonances arise from the intense electromagnetic coupling between closely spaced particles assembled via capillary-driven method onto a sample with with pre-patterned surface (see Figure 2.5c).

For nanoparticles that are not clustered together but are still quite close and mutually interacting, analytical methods to model their optical response are usually employed. It was recently showed by Antosiewicz et al. [68] that using a "film of dipoles" approach, an amorphous array of AuNPs can be modelled, and that controlling the characteristic distance between nanoparticles can be used for tuning the optical response of such arrays. This effect turns up to be universal, proven by similar study on quantum dots with diameters bellow 5 nm [69]. It was also suggested that interaction between nanoparticles in a honeycomb lattice can result in a collective plasmon dispersion relation similar to that of graphene [70]. These examples reveal that analytical calculations can predict and precisely model the optical response of arrays of nanoparticles. In this work, spectroscopic ellipsometry was used for measuring the optical properties of metallic nanoparticles. Although one can utilize analytical approaches similar to those described above to deal with ellipsometric response of arrays and films of particles [71], it is also fairly convenient to employ a theory of effective medium approximation (EMA).

3.4 Effective medium theory in characterization of metallic nanoparticles

Solid state matter, consisting of individual atoms, behaves as a continuum whenever the wavelength of incident light is much larger than the lattice constant. Therefore only smooth averages of its properties are detected whenever light at optical frequencies is used as a probe, in contrast to X-rays which undergo substantial diffraction and can thus reveal the atomic structure. Similarly, when modelling nanostructured materials by EMA, the averaged properties characterizing the whole nanostructure are found by various rules for mixing dielectric functions of its constituents, incorporating their volume fractions, shapes, and orientations. As a result, a system constituted e.g. of interacting metallic nanoparticles is replaced by a homogeneous layer with effective (average) dielectric constant ε_{eff}, representing the overall response of the modelled system (Figure 3.5a). One should be always careful though, as this approximative treatment is valid only when the inner structure length-scale is small compared to the wavelength. The theory behind EMA is not complicated but to keep this text short its description will be limited only to issues directly related to this work. The thorough derivation of several EMA rules as well as a discussion of their applicability in various situations can be found in Ref. [72].

As denoted above, all EMA models for two-phase materials are basically formulae for mixing dielectric functions ε_{a} and ε_{b} of the two components embedded in some host medium ε_{h}, weighted by their volume fractions f_{a} and f_{b}.

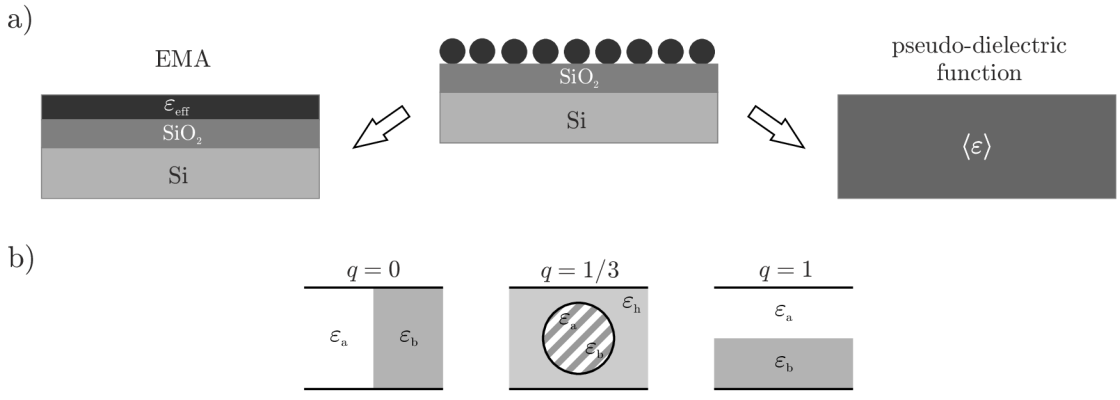

Fig. 3.5: Effective medium approximation. **(a)** Schematic illustration showing how a layer of nanoparticles on the top of a silicon substrate is modelled by an EMA layer with effective dielectric function ε_{eff}. The other option is to use pseudo-dielectric function (will be described in Section 4.3). **(b)** Three types of microstructures corresponding to significant values of a screening factor q in EMA mixtures.

Two standard EMA models have been used in this work — Maxwell Garnett (MG) and Bruggeman (BEMA). The two can be expressed by a single formula [73]:

$$\varepsilon_{\text{eff}} = \frac{\varepsilon_{\text{a}}\varepsilon_{\text{b}} + \kappa\varepsilon_{\text{h}}\left(f_{\text{a}}\varepsilon_{\text{a}} + f_{\text{b}}\varepsilon_{\text{b}}\right)}{\kappa\varepsilon_{\text{h}} + \left(f_{\text{a}}\varepsilon_{\text{b}} + f_{\text{b}}\varepsilon_{\text{a}}\right)}, \tag{3.4}$$

where κ is defined using screening factor q as $\kappa = (1-q)/q$. The MG and BEMA models are described by (3.4) after setting the host medium $\varepsilon_{\text{h}} = \varepsilon_{\text{a}}$ and $\varepsilon_{\text{h}} = \varepsilon_{\text{eff}}$, respectively. The former thus somehow represents the situation when a component "b" is embedded in a host medium "a". The latter, on the other hand, corresponds to a self-consistent case of the host medium being the effective medium itself. The role of the screening factor, which is used to describe the microstructure of constituents in EMA mixtures, is illustrated in Figure 3.5b. As both models were developed assuming spherical dielectric inclusions, the default screening factor is given by $q = 1/3$. Nevertheless, a columnar or laminar microstructure can be modelled by setting screening factor q to zero or one, respectively.

Before the application of these models to layers of nanoparticles will be shown, the method used in this work for measuring of optical constants of such systems — the spectroscopic ellipsometry — will be briefly described.

3.5 Spectroscopic ellipsometry

Spectroscopic ellipsometry is a method of optical characterization of materials, their surfaces, and thin films. It is based on measurements of change in polarization of light after its reflection from the sample of interest. Both amplitude and phase of the two (s- and p-) components of the electric field vector [74] are in general altered by this reflection and optical properties of the sample are "imprinted" to the state of polarization after reflection.

Ellipsometry can be done in various experimental configurations. Measurements in this work were done using J. A. Woollam VASE ellipsometer, which uses rotating analyzer configuration combined with a computer controlled retarder element (compensator) — see Figure 3.6. In this setup, unpolarized light from a xenon lamp passes through a monochromator to fixed polarizer (Glan-Taylor type) and retarder plate which in turn select wavelength and polarization state of light incident on the sample. The angle of incidence is set by a motor-driven goniometer and the polarization after reflection from the sample is extracted from light passing through a rotating analyzer (Rochon type) or, more precisely, from its intensity at the detector (Silicon InGaAs photodiode pair) as a function of the analyzer angle.

The outcome of the measurement are spectra of two ellipsometric parameters ψ and Δ characterizing the sample optical properties, usually for several angles

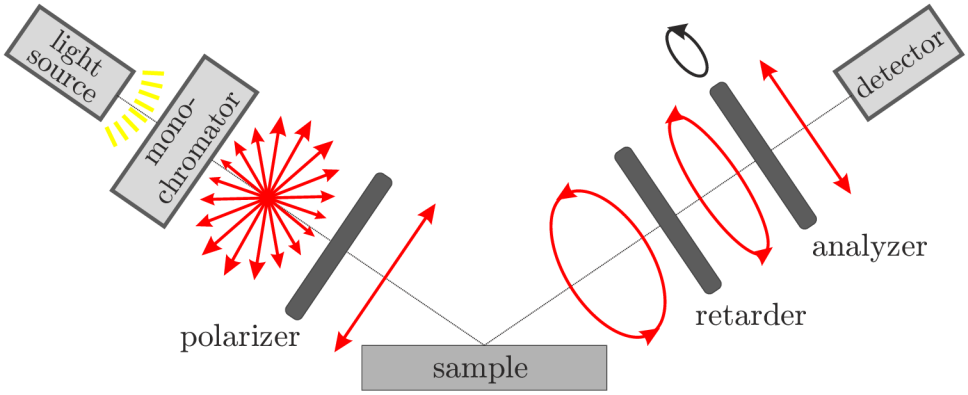

Fig. 3.6: Schematic illustration of spectroscopic ellipsometry setup with rotating analyzer and retarder. Unpolarized light from light source and monochromator passes through a polarizer, reflects on the sample and its polarization state is changed. Then it passes through a retarder, which shifts the phase, and after crossing another polarizer (called analyzer, to avoid confusion) it hits the detector. From the light intensity as a function of rotational angle of polarizer one can calculate ellipsometric parameters ψ and Δ characterizing the change of polarization upon reflection.

of incidence. These parameters are defined from the ratio of complex amplitude reflection coefficients for s- and p-polarizations of the light wave, r_s and r_p, as follows:

$$\rho \equiv \tan\psi \exp(\mathrm{i}\Delta) \equiv \frac{r_\mathrm{p}}{r_\mathrm{s}}. \tag{3.5}$$

This equation shows tight relationship between measured parameters and reflection coefficients (i.e. optical properties of the sample). Namely, ψ is associated with the amplitude part of the reflection coefficients and Δ with the phase part.

For samples representing a semi-infinite interface, the complex dielectric function of their material can be directly extracted from measured data. For more complicated samples, however, one must find a model which will reproduce ψ and Δ spectra matching those experimentally obtained (so called fitting). The main features of this process are a) implementing the knowledge of the sample structure (e.g. number of layers), dimensions of the constituent entities (e.g. thicknesses of layers), optical properties of the constituent structures (e.g. dielectric function of known layers), etc., and b) numerical methods for minimizing mean squared error (MSE) of the fit compared to the measured data. The complexity of this process closely follows that of the sample structure and while it is quite straightforward in the case of simple substrate-film systems, it may become troublesome when dealing with samples of unknown structure or composition.

3.6 Analysis of films of metallic nanoparticles by ellipsometry

Ellipsometry was chosen for analysis of random assemblies of AuNPs due to its excellent sensitivity towards optical properties and structural differences. Three samples denoted as Au20, Au40, and Au60 were cut from the wafer of sample B type and partly immersed for 2 h in colloidal solutions of AuNPs with corresponding mean diameter of 20, 40, and 60 nm. The first solution was modified by 2.5 mM hydrofluoric acid and the second two were both modified by 2.7 mM hydrochloric acid for reasons described in Ref. [75]. The partial immersion was done in order to keep a clean silicon surface as a reference. After the deposition, uniformity of nanoparticle film was verified by SEM (Tescan Lyra) and representative images are presented in Figure 3.7a. Both covered and clean parts of all samples were then measured by ellipsometric setup described in the previous section at three angles of incidence (65°, 70°, 75°) in a wavelength range of 400–1000 nm. Experimental results (plotted in Figure 3.7b) were fitted using models discussed below.

To obtain reasonable background for future analysis of nanoparticle films, the data measured on reference (silicon) samples were fitted for the thickness of silicon oxide. This is quite routine and simple process as the optical properties of both silicon and its native oxide are very well described for wafers manufactured using standard procedures. Indeed the thickness of the oxide was determined to be 1.8 ± 0.1 nm for all three samples using fit with MSE < 1, indicating almost perfect match. Let us note that such a high precision of thickness measurements is quite common in ellipsometric studies of similar systems [76], confirming its potential for thin films analysis.

The model for silicon substrate and the thin layer of its oxide was then fixed and an EMA layer was added on the top of them. This layer comprised two components: gold with bulk dielectric function obtained from ellipsometer software library (values reprinted in Appendix A) and volume fraction f_{Au}, and vacuum with dielectric function equal to one and volume fraction $(1 - f_{\mathrm{Au}})$. The unknown variables which were set free during minimization procedure were the thickness t of the EMA layer, the volume fraction f_{Au}, and in some cases also the screening factor q. It should be emphasized that when using conventional minimization algorithm there is often a risk of fitting result being only local minimum in an N-dimensional space of N fitting variables. For this reason, a global minima search was performed using software feature of VASE ellipsometer. This promised correct results even in situations when strong correlation of parameters makes conventional fitting uncertain (which is the case when the screening factor q together with either t or f_{Au} are set free [77]).

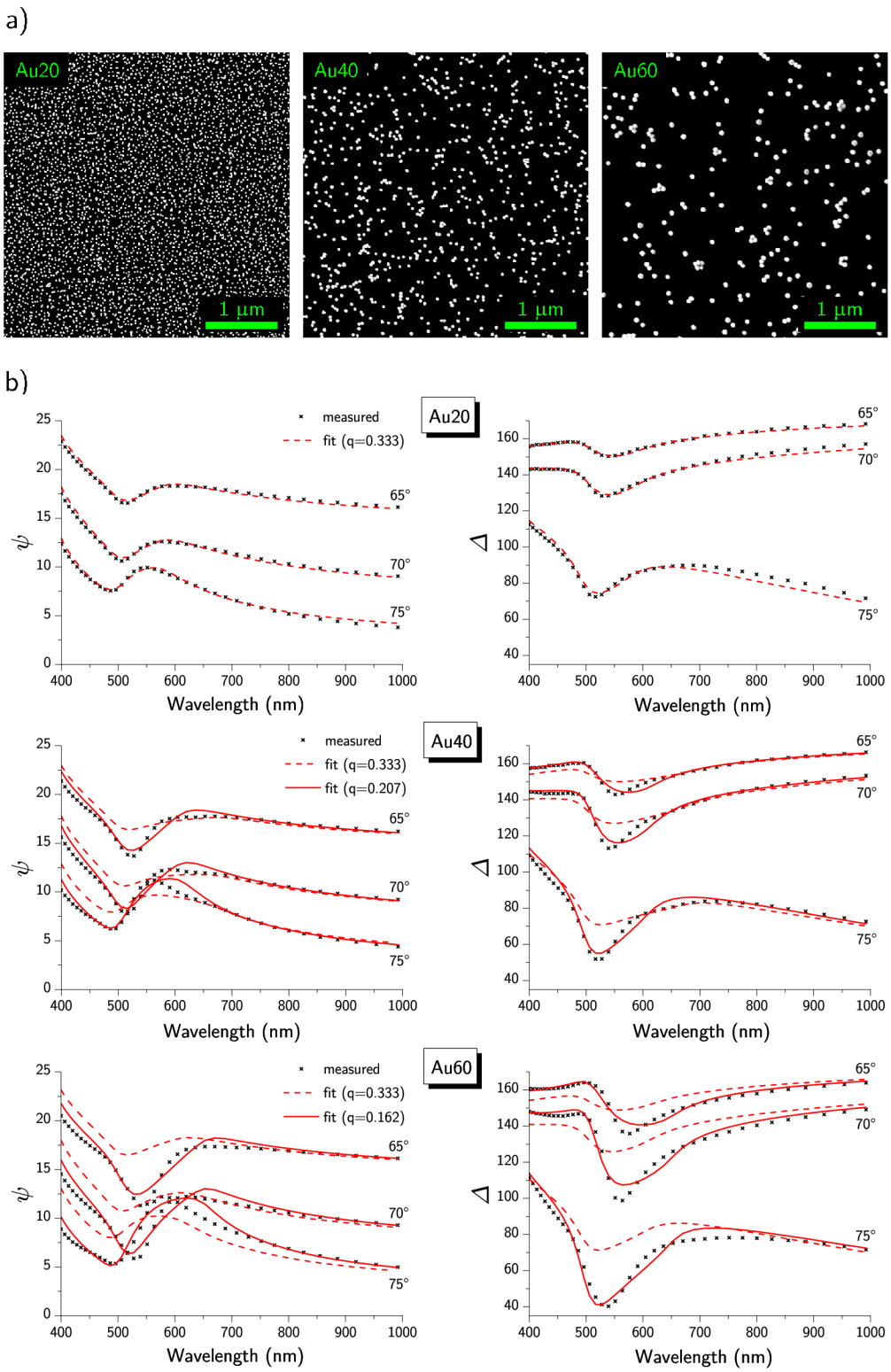

Fig. 3.7: Fitting of ellipsometric spectra by means of Bruggeman's EMA. **(a)** SEM micrographs of samples covered by AuNPs with diameters 20, 40, 60 nm denoted as Au20, Au40, Au60, respectively. **(b)** Ellipsometric spectra of the samples measured at three angles of incidence. Crosses correspond to measured data, dashed red lines are fits using standard screen factor $q = 1/3$, solid red lines are fits with the screen factor unfixed. The fitting parameters are summarized in Table 3.1.

Tab. 3.1: A summary of parameters used in BEMA fits of ellipsometric spectra from Figure 3.7. The best MSE achieved by equivalent MG fit is appended for comparison.

sample	q	t (nm)	f_{Au} (%)	f_{obs} (%)	MSE	MSE of MG
Au20	0.33 (fixed)	19.3 ± 0.6	8.3 ± 0.3	7 ± 0.5	6.3	22
Au40	0.33 (fixed)	14 ± 1	13 ± 1	4 ± 1	24.3	49
	0.207 ± 0.004	31 ± 2	3.4 ± 0.2	4 ± 1	9.8	15
Au60	0.33 (fixed)	18 ± 3	10 ± 2	3 ± 1	72.4	110
	0.162 ± 0.003	36 ± 2	2.4 ± 0.2	3 ± 1	20	41

Both MG and BEMA mixing rules described in previous section have been tested for their applicability in modelling nanoparticle layers on solid substrates. Although MG model was originally developed for media containing "minute metal spheres" [78] and was also suggested as more appropriate for modelling ellipsometric spectra of AuNP films [79], in this study the BEMA approach outperformed it in all cases (see MSE values in Table 3.1. In fact, for the smallest nanoparticles it was expected as the distances between nanoparticles are quite small and their concentration is most likely out of the dilute limit of MG model. Even though the surface coverage of larger nanoparticles is quite low, their interparticle distance (relative to their diameter) is not that large and an assumption of only far-field interaction among them is probably not valid, which results in limited validity of MG approach [64].

The fits of ellipsometric spectra by models employing BEMA are plotted in Figure 3.7 and their parameters are summarized in Table 3.1. The best results were achieved for sample Au20 which is evident when comparing corresponding experimental and modelled spectra by MSE. The thickness of the layer is also in excellent agreement with mean diameter of the nanoparticles, as it should be since the voids between nanoparticles are already covered by low volume fraction of gold. To verify the accuracy of f_{Au} obtained from fit, the surface coverage by AuNPs was counted for all three samples from SEM images (Figure 3.7a) and an "observed" volume fraction f_{obs} was calculated (see Table 3.1). The results are again in good agreement, implying applicability of BEMA to model ellipsometric spectra of small nanoparticles.

The quality of the fit deteriorates for larger nanoparticles, especially in regions of plasmon resonance (500–600 nm, where a characteristic "dip" is visible in otherwise smooth ψ and Δ spectra), suggesting that our model could not account for change in either their diameter or arrangement. Also the thicknesses of both EMA

layers were physically incorrect as well as respective volume fractions. To improve the performance of the model, the screening factor q was set free for minimization. This step indeed resulted in substantial improve of both fits, represented by better fit performance around plasmon resonance and by a 60 % drop of MSE. The volume fractions again matched those observed on real samples and the thicknesses, although being somewhat underestimated, were much closer to their expected values. To qualitatively understand the influence of screening factor it is necessary to compare Figure 3.5b with SEM images of samples Au40 and Au60 in Figure 3.7a. The images reveal how the films of larger nanoparticles turn to being considerably inhomogeneous on the scale of a single wavelength (approximately half of the respective scale bar). The effective medium is thus no longer well-represented by spherical inclusions corresponding to screening factor $q = 1/3$, and it should be getting closer to the columnar limit of $q = 0$, which is exactly the case of our fitting procedure. Lower screening factor also means that ε_{eff} is more influenced by the phase with higher dielectric constant [73], which could also account for improved fit performance in the resonance region.

In the first part of this chapter it has been shown how unique optical properties of metallic nanoparticles arise from the theory of electromagnetism and can be studied using various analytical and numerical methods. The optical properties of ensembles of nanoparticles are especially important in the context of previous chapter where our abilities to control dimensions and geometry of such structures have been demonstrated. Two powerful components of thin (metal nanoparticle) film analysis have been also described — spectroscopic ellipsometry, as the measurement tool, and effective medium approximation, as the tool for modelling the optical properties. It was also demonstrated that by combining these two methods one can successfully assess the quality of nanoparticle films. The optical properties of ordered arrays of nanoparticles have been also investigated during this study, mainly by means of microscopic reflectometry, but partly because experimental difficulties the results were not reliable and conclusive. Future work have thus to be addressed to improve this aspect of nanoparticle analysis as it is crucial for further investigation of nanoparticle clusters fabrication. In the following chapter we will introduce sensing devices which are based on the optical properties of systems containing metallic nanoparticles and also attempt to employ ellipsometry in detection of short DNA molecules.

4 BIOSENSORS

Fast, effective and low-cost biosensors are essential for future progress in all fields of medical care. The next generation of these devices should facilitate real-time identification of various types of biomarkers, including proteins or nucleic acids, all in an automated way. The concept of the biomedical device with a plasmonics-enabled detection scheme was recently summed up by Brolo [80]:

> Raw biological sample is injected into the front end part of the device. Several biochemical operations, including filtration, blood separation and amplification by polymerase chain reaction, have been adapted for microfluidic implementation. After treatment, the sample is directed to a sensing region containing several plasmonic elements that can be simultaneously interrogated for multiple analytes. Using arrays of nanoholes or nanoparticles, the excitation and detection of SPR can be realized in a collinear arrangement using low-cost light-emitting diode and a camera.

To achieve this goal, a progress in microfluidical manipulation, automated biochemical operations, and optoelectronics is crucial. In the optoelectronic part, an application of plasmonics seems to provide promising outcomes which can result in its implementation to the future generation of health care devices.

4.1 Plasmonics-based biosensors

Historically, pioneering plasmonic biosensors were based on propagating form of surface plasmons. These excitations are bound to a metal-dielectric interface (similar to conventional waveguides), because their wavevector is larger than that of light in the dielectric. It is also the reason why an excitation of these modes is possible only when a wavevector mismatch is overcome by means of surface inhomogeneities (gratings) or prism coupling [81]. The latter scheme, sometimes called attenuated total reflection, is fundamental for vast amount of existing plasmonic biosensors. Typically, it is achieved in the Kretschmann configuration (Figure 4.1), where a thin metal film on one side of a glass prism is used for excitation of SPP on the metal-dielectric interface. That results in a resonant transfer of incident light energy into the SPP and the resonance condition can be detected by measuring the intensity of reflected light as a function of either time, wavelength, or incident angle. Since the first demonstration of the use of SPR for gas detection and biosensing in 1982, many applications of SPR-based sensing devices have been described. In 1990 some have even become commercially available (Biacore, Horiba Scientific, IBIS Technologies, etc.)

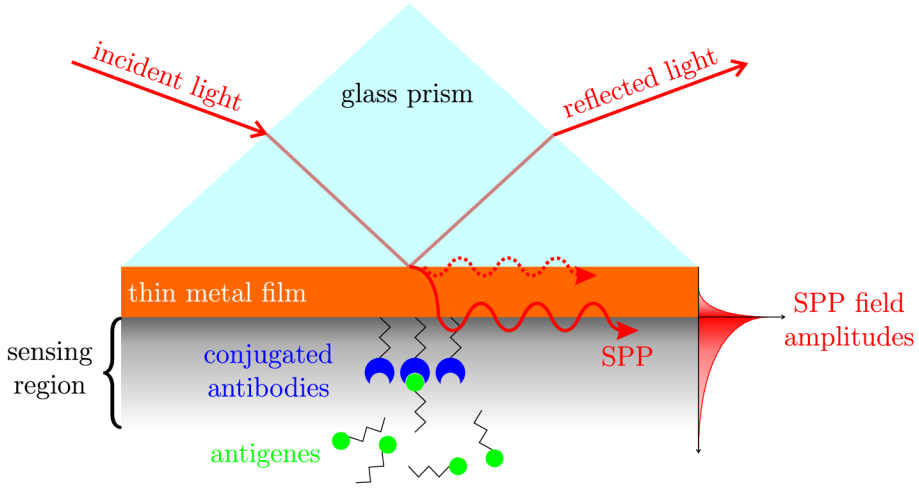

Fig. 4.1: Plasmonic biosensing in the Kretschmann configuration. A collimated incident light beam is totally reflected at the prism-metal interface, while it excites the SPP at the outer boundary of the metal by evanescently propagating through the thin film. The resonance manifest itself by a large drop in reflected light intensity. The incident angle or wavelength at which the resonance occurs depends profoundly on the refractive index of material within the field penetration depth. To achieve the selectivity of the biosensor towards particular molecule, the surface is often functionalized by some chemical recognition elements (e.g. antibodies) which represent chemical counterparts for the target molecules (e.g. antigenes). The binding event causes a change of resonance condition which can be detected as a shift of resonance angle (for given wavelength) or resonance wavelength (for given angle).

The electromagnetic field of SPP decays exponentially with distance from the surface (Figure 4.1). Because of that, there is strong confinement of the field to the vicinity of the interface (hundreds of nanometers for gold film, depending on wavelength [82]), and the SPR condition is very sensitive to variations in the optical properties of the dielectric superstrate. Plasmonics-based detection is thus, in fact, measurement of changes in the effective refractive index within the field penetration depth of SPP.

Although these measurements are not specific to molecules of choice, the biosensor is usually made highly selective to the particular biomolecule by some sort of surface chemistry modification: a chemical counterpart to the required target is immobilized on the surface of metallic film and a change in signal is detected only when the target molecules bind to them. Non-specific binding is prohibited by steric or electrostatic barrier and bulk changes far away from the surface, which are of no interest in the particular biosensor, are effectively suppressed.

The use of localised SPR for biosensing offers one promising advantage over the propagating plasmons: the sensing region is much smaller as the field penetration

depth is 40–50 times shorter than that of conventional SPR sensors [57]. For spherical nanoparticles, for example, all reported sensing depth estimations appear to be within 1–2 particle diameters [83]. It should be emphasized that all attributes of electric field in the vicinity of nanoparticles can no longer be described by simple exponential decay. The penetration depth is thus not the exact measure of the field strength in that case. It still holds, however, that LSPR is less susceptible to impurities and inhomogeneities in bulk environment and probes only changes occurring on the surface and up to few tens of nanometers away from it, whereas SPR detects changes up to the distance of hundreds of nanometers from the surface. Moreover, advances in both bottom-up and top-down fabrication techniques allow us to move the LSPR wavelength from visible to the infrared part of the electromagnetic spectrum (see Figure 3.3). This means we can tune the resonance to a region which is the most appropriate for given analyte or make its linewidth narrower to increase the sensitivity. An example demonstrating the importance of such precise control was given by Haes et al. [84] by optimizing the LSPR-shift response to a specific substance of interest.

Although ensembles of nanoparticles are the typical choice for application of LSPR in biosensing, single nanoparticle LSPR spectroscopy is another option, offering sensitivity comparable to that of nanoparticle-array-based LSPR spectroscopy. For example, triangular nanoprisms functionalized with alkanethiols of increasing chain length show a 4.4 nm shift in maximum LSPR wavelength per each additional CH_2 group of adsorbed molecules, thus offering a very high single-particle refractive-index sensitivity [85]. Owing to the small dimensions of single nanoparticles, there is a potential for fabrication of miniature immunoassays for multiplex (parallel) testing on less-than-micrometer scale [86]. Although high-end SPR instrumentation is still bulky and not suitable for portable employment, it will provide performance benchmark to novel miniature biosensors and new plasmonic based platforms should thus outperform it in order to succeed.

To test the possibility of employing arrays of nanoparticles in biomolecule sensing, the samples from Section 3.6 have been conjugated with oligonucleotides, i.e. short, single-stranded DNA molecules. The basics of this bioconjugation process will be briefly outlined below.

4.2 Bioconjugation strategies for gold nanoparticles

The bioconjugation chemistries are usually driven by the nanoparticle surface, the stabilizing ligand, or some functional intermediary. These three stages also corre-

Tab. 4.1: Selected applications of representative nanoparticles-bioconjugates. After [87].

nanoparticle	biological	application	reference
gold	DNA	templated assembly, diagnostics	[88, 89]
gold	proteins/enzymes	bioelectronics	[88]
gold	carbohydrate/peptide	cellular labelling	[89]
gold	lipid/DNA	gene therapy	[90]
silver	antiamyloid ligand	Alzheimer's detection	[91]
silver	antibodies	cell surface detection	[91]

spond to increasing number of possible conjugates: There are not many chemical groups that will assure selective and secure binding of other molecules to the surface of nanoparticles from particular material. Therefore the chemistry of stabilizing ligands, which are inherent to all nanoparticles, is often used to drive the bioconjugation. The limitations are quite straightforward; not every conceivable ligand necessary for particular bioconjugate is suitable for nanoparticles preparation and vice versa. So sometimes complicated chemical procedures have to be carried out with uncertain results. The alternative way is to bind the target biomolecule not directly to nanoparticle's ligands but rather to some functional intermediary which contains chemical groups suitable for connecting the two. One can imagine that this approach offers almost infinite number of possibilities how to functionalize a surface of metallic nanoparticles. For more profound insight into this subject we refer to a recent review by Sapsford et al. [87].

The cost of an increased selectivity and wider range of detectable substances is that these are getting much farther from the surface of nanoparticle, out of the region of high field intensity. This is particularly important for nanoparticles stabilized by very long molecules (e.g. polymers) because the benefits of special nanoparticle's properties may diminish. In the case of citrate-stabilized AuNPs the situation is much less complicated thanks to the thiol chemistry. The affinity of molecules with a thiol group ($-$SH) towards gold surfaces is known for a very long time but although "the chemistry involved for the chemisorption of thiols on gold is, in principle, the most straightforward" it "remains the most enigmatic" up to the present time [92]. Keeping in mind that the details regarding some aspects of the gold-thiol interaction might be unclear, one can still take an advantage from the strength of the Au$-$S bond and utilize it in biosensing. This is especially true for proteins, peptides, and DNA, where thiolate chemisorption forms the predominant basis of their conjugation with AuNPs.

To test the application of nanoparticle films in biosensing, the experiment was designed in close cooperation with team of doc. Fojta from Institute of Biophysics AS CR: 38-bases-long thiolated oligonucleotides[1] with a binding site for protein p53 [93] have been prepared for attachment to AuNPs.

The functionalization of AuNPs in their colloidal solutions has been satisfactorily described in a pioneering work by group of C. A. Mirkin [94]. Their procedure resides in simple mixing of cleaved and purified oligonucleotides with the colloidal solution of AuNPs and subsequent salting, i.e. sequential adding of NaCl up to the concentration of 1 M, followed by incubation overnight. High concentration of NaCl helps to screen the negative charge carried by both DNA and AuNPs, but it can also induce irreversible aggregation of AuNPs. Therefore it has to be added in a step-wise manner to provide enough time for DNA to adsorb and thus stabilize the nanoparticles (the high concentration of salt is not a problem for DNA-stabilized nanoparticles as there is also a steric barrier preventing their aggregation).

In our case, unfortunately, it was not favourable to functionalize nanoparticles in solution prior to their assembly on silicon substrate, because the layer of DNA on the surface of AuNPs would not be compatible with the process of deposition described in Section 2.3. Especially, the treatment with hydrofluoric acid could be harmful to the DNA, altering its conformation and functionality. On account of that we decided to examine the loading of DNA to the layer of nanoparticles which had been already immobilized on the surface. Such approach may provoke doubts of the oligonucleotides being adsorbed not via chemisorption but only due to weak electrostatic or van der Waals interactions. This non-specific binding of DNA, recently investigated by group of J. Liu [95], may be detrimental for the designated function of our oligonucleotides (the hybridization of complementary strands of DNA or binding of protein p53) and it must be addressed by more experiments in the future.

Bearing in mind the facts mentioned above and also results of our early experiment conducted some time ago, we have decided to test a following procedure of AuNPs' functionalization: An aqueous solution of oligonucleotides with concentration of 30 µg/ml was drop-casted onto the samples Au20/Au40/Au60, which were fabricated and inspected as described in Section 3.6. To assure the droplet will not evaporate and vanish, leaving the clumps of the dried DNA behind, the samples were kept in a chamber with stable humidity of 95 % for 24 h. After this treatment the droplet was washed away and samples were thoroughly rinsed in ultrapure water and gently dried in a stream of nitrogen gas. Finally, they were all measured by spectroscopic ellipsometry in the same configuration as in the previous case.

[1] The sequence was 5'-AAG**AGGCATGTCTAGGCATGTCT**CTTGATATCGAATTC−SH with a p53 binding site marked bold.

4.3 Ellipsometric detection of oligonucleotides

Results of the ellipsometric measurements on the samples described in the previous section are plotted in Figure 4.2a in a form of real and imaginary parts of pseudo-refractive indices. Pseudo-refractive index (or pseudo-dielectric function, which are both equivalent to each other) is a form of ellipsometric spectra often used in ellipsometry to better visualize them. The idea behind is similar to that of EMA (see Figure 3.5a), where the layer of nanoparticles is modelled by a uniform layer with some effective dielectric function. In the case of pseudo- optical constants, the whole sample (i.e. silicon substrate and everything on it) is modelled as one solid body characterized by its appropriate pseudodielectric function. It should be emphasized that it is not true modelling but merely another representation of measured ellipsometric spectra, which is somehow more explanatory because it shows directly the optical properties (of a whole sample), which can be easily put in the context of other fields of optics apart from ellipsometry.

Although they can be found elsewhere [73], the equations describing relationship between ψ and Δ and complex pseudo-dielectric function $\langle\varepsilon\rangle$ at a specific angle θ_i, will be reprinted here to support the statement about their interchangeability from previous paragraph:

$$\langle\varepsilon\rangle \equiv \sin^2\theta_\mathrm{i}\left\{1+\tan^2\theta_\mathrm{i}\left[\frac{1-\tan\psi\exp(\mathrm{i}\Delta)}{1+\tan\psi\exp(\mathrm{i}\Delta)}\right]^2\right\}. \tag{4.1}$$

Additionally, relations between individual parts of dielectric function $\varepsilon \equiv \varepsilon_1 - \mathrm{i}\varepsilon_2$ and refractive index $N \equiv n - \mathrm{i}k$, which also hold for their pseudo- equivalents, will be for completeness reprinted as well:

$$\varepsilon_1 = n^2 - k^2 \tag{4.2a}$$

$$\varepsilon_2 = 2nk. \tag{4.2b}$$

A significant effect of the AuNP layer on ellipsometric spectra (spectra of pseudo-refractive index, more precisely) is evident once again when comparing black (Si without AuNPs) and blue (Si with AuNPs) lines in Figure 4.2. The data from measurements after functionalization of AuNPs by oligonucleotides are plotted in the same graphs in red. The changes of spectra after functionalization are much less profound, which was expected, as the amount of DNA is low and its optical properties are less influential. But at least in the case of Au20 the change is substantial and it would be very useful to somehow extract the properties of the DNA layer out of the background of silicon substrate and AuNP layer. But this is almost impossible to do using standard fitting procedures, due to a minute amount of the DNA on the

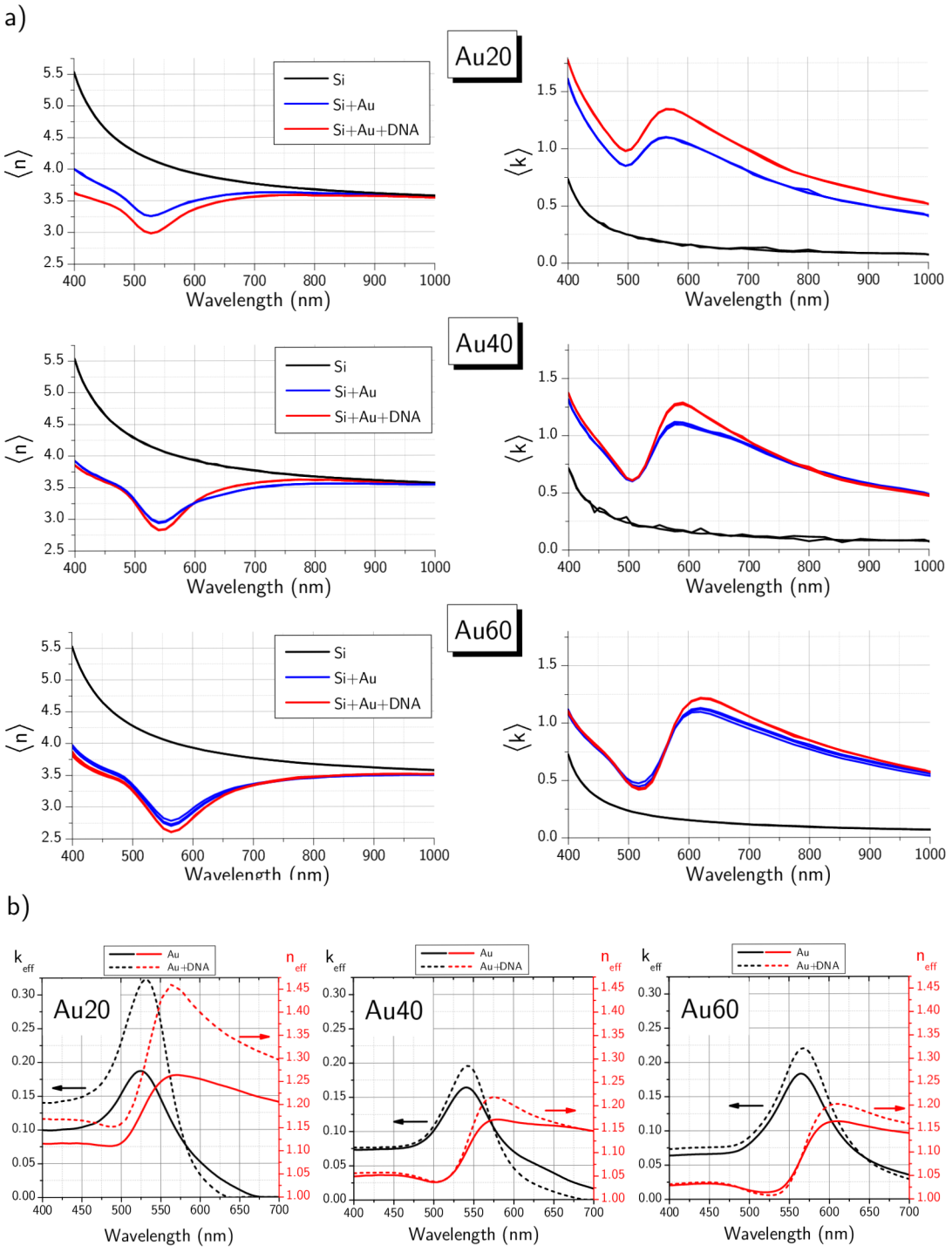

Fig. 4.2: Ellipsometric detection of oligonucleotides. **(a)** The measured spectra of real and imaginary parts of pseudorefractive indices $\langle n \rangle$ and $\langle k \rangle$ corresponding to samples Au20, Au40, and Au60: bare silicon surface (black), surface covered with AuNPs (blue) and surface with AuNPs functionalized by oligonucleotides (red). Every line actually consists of three overlapping lines corresponding to three angles of incidence; this overlapping is a sign of correct measurement. **(b)** Spectra of real (red) and imaginary (black) parts of effective refractive indices obtained from point-by-point fits of data from a). Solid lines are before functionalization, dashed lines are after functionalization by DNA.

sample and its uncharted optical constants. Therefore, an unconventional approach of point-by-point fit was chosen to visualize the change, while making use of the perfect ellipsometric modelling of the empty silicon samples.

Point-by-point fit is the least reliable method of ellipsometric spectra fitting, which is also the least beneficial. In this method, the layer of interest is described by a set of starting optical constants, which are then adjusted (fitted) independently at every wavelength so that the optical properties of the sample match those experimentally obtained. The weakest link of the point-by-point approach is the independent tuning of optical constants which is physically incorrect because these are bound together by Kramers-Kronig (KK) relations [96]. Therefore the results should be always tested for KK consistency. The other disadvantage is that apart from effective optical constants, point-by-point fit does not provide any additional information about inner structure or other properties of the layer of interest. At this stage, point-by-point fitting suits our purposes, as the fit quality is usually very high and we are not yet interested in any characteristics of the DNA at this stage.

As a basis for this analysis, results of samples Au20, Au40, and Au60 fitting from Section 3.6 (summarized in Table 3.1) were taken as a starting point. Namely, the thicknesses of layers were fixed and optical constants corresponding to the results produced by BEMA mixing were then adjusted at every wavelength. This way we obtained excellent fits with MSE ≈ 1 and effective refractive indices of AuNP layers both before and after functionalization by the DNA (plotted in Figure 4.2a as real part n_{eff} and imaginary part k_{eff}).

Since the starting points were taken from high-quality fits with physically correct background the results were expected to be physically correct as well. The effective indices resulting from point-by-point fits were also tested for KK consistency and all passed with very high level of certainty. It is worth noting that the results are also in agreement with previously stated red-shift of plasmon resonance: compare the shift of k_{eff} peaks (which are associated with absorption by definition) corresponding to increasing nanoparticle diameter in Figure 4.2 with the shift of absorbance spectra in Figure 3.2. The changes of spectra after functionalization were the largest in the case of sample Au20. The values of effective refractive index have been almost doubled and the peak position of k_{eff} was shifted by 7 nm. Although the change in the measured spectra of samples Au40 and Au60 is noticeable and by all means out of the measurement uncertainty, the results of fitting analysis are not entirely conclusive. The change in the amplitude of the peaks is significant, but its interpretation is problematic. The shift of the peak positions towards larger wavelengths (1–3 nm) is also detectable.

We can infer from the results plotted in Figure 4.2 that ellipsometry is indeed a very sensitive technique, even towards subtle changes of surface optical properties caused by adsorption of short DNA molecules. Using modelling methods described in this thesis (EMA, point-by-point fit) we can investigate these minute variations in more detail. Further experiments have to be conducted, investigating e.g. the way how oligonucleotides attach to the surface or whether they are positioned so that hybridization with complementary strands or binding of proteins is allowed. However, the proof-of-concept demonstration is provided here and these findings will serve as a starting point for future work on this topic.

5 CONCLUSIONS

Prior work in the field of metallic nanoparticles has documented that it is possible and useful to utilize their attractive properties in various applications including detection of whole range of biomolecules. Although many studies make use of nanoparticles in their colloidal solutions, one can enhance and control their function even more by their immobilization onto solid substrates. Yet to the best of our knowledge, to achieve this goal all previous studies need some sort of serious modification of the substrate surface, either in chemical or topographic sense.

In this thesis we have presented a novel approach to the self-assembly of AuNPs onto silicon substrates. It has been demonstrated that by careful adjustment of pH, affinity of AuNPs towards silicon surface can be significantly promoted. Based on the principle introduced in previously published article it has been shown that altering the surface chemistry can be done also using electron beam irradiation and it is possible to achieve the self-assembly into ordered structures. Examples of resulting shapes included precisely defined circular arrays of AuNPs or nanoparticle grids.

These new findings extend those already published by our group, demonstrating that by employing electron beam, similar level of precision as in the case of ion irradiation can be achieved. In the case of electrons it seems that the intersection of applicable fluences and irradiated area dimensions is slightly narrower than in the case of ions. Therefore the use of electrons demands increased experimental experience. Nevertheless, damage to the surface is not an issue anymore, which is in sharp contrast with the possible contamination of the surface by implanted ions or even undesirable destruction of the surface topography by ion sputtering. Electron beam patterning can thus serve as a foundation for fabrication of nanoparticle ensembles with excellent precision without any uncertainty about purity of the surface. On top of that, grids of irradiated spots with carefully designed shapes can be fabricated owing to the small dimensions of electron beam. Such patterns could facilitate the assembly of nanoparticle clusters with desired morphology (e.g. chains or heptamers). Future work should be addressed towards fine-tuning of this aspect of patterning as well as towards improving lateral resolution of assembled structures which is currently approaching 100 nm (a value similar to the one achieved by ions).

AuNPs are well known for their distinctive optical properties, particularly because of their resonant response to the incident light in the visible part of electromagnetic spectrum. On account of that, the second part of this thesis covers the major aspects of metallic nanoparticles optical properties, including assessment of Mie's theoretical approach towards this topic, and its possible limitations. It has also been shown that thanks to the progress in nanoparticle preparation, theories and numerical methods which can explain optical behaviour of nanoparticles with

non-spherical shapes have to be employed nowadays. Additionally, our ability to organize nanoparticles calls for methods which can also cope with optical properties of nanoparticle ensembles.

The collective properties of non-interacting nanoparticles in solutions or in very sparse layers can be successfully described as the multiplication of single nanoparticle optical response. When dealing with nanoparticle clusters or their dense layers, though, the mutual interactions strongly influence the optical response of nanoparticles both in near and far fields. A noteworthy subset of methods which can handle this task, namely the effective media approximations, have been used in this study to model experimental data measured by spectroscopic ellipsometry. It has been shown that we can estimate the thickness and density of nanoparticle layer on top of solid substrates with very good accuracy. These findings notably extend those published in author's bachelor's thesis, and demonstrate the idea that superior sensitivity of spectroscopic ellipsometry towards changes on surfaces can be used for analysis of metal nanoparticle thin films.

To use this method for analysis of nanoparticle ensembles, it is always necessary to focus the light to the structures of interest as the large scale fabrication is still a problem. An ellipsometer with focusing probes (down to 100 µm illumination spot) and translation stage could suit this purposes, yet such was currently not available. Reflectometry, both in a conventional setup on optical table and within optical microscope, was also tested while working on this thesis, but the results were not trustworthy and often physically incorrect. Therefore an important task for future studies is to find a method which will be able to investigate properties of nanoparticle ensembles in fast and reliable way.

The remarkable optical properties of metallic thin films have been employed for detection of biomolecules long time ago. However, to make use of metallic nanoparticles in biosensing still remains a challenge. In the last part of this thesis the classical sensing schemes based on plasmonics have been described, since these set the benchmark of quality for newly developed devices. The key step in making the sensors molecule specific is a functionalization of the sensing structures, which has been briefly outlined and also investigated by an experiment with thiolated oligonucleotides. Apparent shift of the ellipsometric data together with the successful test of point-by-point fit applicability provided compelling evidence for employment of spectroscopic ellipsometry in the field of plasmonic biosensing.

More experiments have to be conducted to verify the robustness of this method, its susceptibility towards non-specific interactions and its sensitivity in further stages of sensing applications such as evaluation of DNA-protein interactions or hybridization of complementary single stranded DNAs.

Our ability to fabricate precisely defined arrays and clusters of nanoparticles,

followed by finding suitable method for their analysis and especially evaluation of their optical properties may provide starting point for fabrication of novel sensing devices, which could compete with state of the art sensors in terms of more significant response or smaller dimensions.

BIBLIOGRAPHY

[1] Zeng, S., Yong, K.-T., Roy, I., Dinh, X.-Q., Yu, X., and Luan, F. A Review on Functionalized Gold Nanoparticles for Biosensing Applications. *Plasmonics*, 6 (3), **2011**, pp. 491–506. doi:10.1007/s11468-011-9228-1.

[2] Losurdo, M., Giangregorio, M. M., Bianco, G. V., Suvorova, A. A., Kong, C., Rubanov, S., Capezzuto, P., Humlicek, J., and Bruno, G. Size dependence of the dielectric function of silicon-supported plasmonic gold nanoparticles. *Physical Review B*, 82, **2010**, p. 155451. doi:10.1103/PhysRevB.82.155451.

[3] Atwater, H. A. and Polman, A. Plasmonics for improved photovoltaic devices. *Nature Materials*, 9 (3), **2010**, pp. 205–213. doi:10.1038/nmat2629.

[4] Schmidt, V., Wittemann, J. V., Senz, S., and Gösele, U. Silicon Nanowires: A Review on Aspects of their Growth and their Electrical Properties. *Advanced Materials*, 21 (25-26), **2009**, pp. 2681–2702. doi:10.1002/adma.200803754.

[5] Maier, S. A., Kik, P. G., Atwater, H. A., Meltzer, S., Harel, E., Koel, B. E., and Requicha, A. A. Local detection of electromagnetic energy transport below the diffraction limit in metal nanoparticle plasmon waveguides. *Nature Materials*, 2 (4), **2003**, pp. 229–232. doi:10.1038/nmat852.

[6] Schmitt, J., Mächtle, P., Eck, D., Möhwald, H., and Helm, C. A. Preparation and Optical Properties of Colloidal Gold Monolayers. *Langmuir*, 15 (9), **1999**, pp. 3256–3266. doi:10.1021/la981078k.

[7] Kolíbal, M., Konečný, M., Ligmajer, F., Škoda, D., Vystavěl, T., Zlámal, J., Varga, P., and Šikola, T. Guided Assembly of Gold Colloidal Nanoparticles on Silicon Substrates Prepatterned by Charged Particle Beams. *ACS Nano*, 6 (11), **2012**, pp. 10098–10106. doi:10.1021/nn3038226.

[8] Faraday, M. The Bakerian Lecture: Experimental Relations of Gold (and Other Metals) to Light. *Philosophical Transactions of the Royal Society of London*, 147, **1857**, pp. 145–181. doi:10.1098/rstl.1857.0011.

[9] Barth, J. V., Costantini, G., and Kern, K. Engineering atomic and molecular nanostructures at surfaces. *Nature*, 437, **2005**, pp. 671–679.

[10] Jin, Y. Engineering Plasmonic Gold Nanostructures and Metamaterials for Biosensing and Nanomedicine. *Advanced Materials*, 24 (38), **2012**, pp. 5153–5165. doi:10.1002/adma.201200622.

[11] Turkevich, J., Stevenson, P. C., and Hillier, J. A study of the nucleation and growth processes in the synthesis of colloidal gold. *Discussions of the Faraday Society*, 11, **1951**, pp. 55–75. doi:10.1039/DF9511100055.

[12] Zhao, P., Li, N., and Astruc, D. State of the art in gold nanoparticle synthesis. *Coordination Chemistry Reviews*, 257, **2013**, pp. 638–665. doi:10.1016/j.ccr.2012.09.002.

[13] Frens, G. Controlled nucleation for the regulation of the particle size in monodisperse gold suspensions. *Nature Physical Science*, 241, **1973**, pp. 20–22. doi:10.1038/physci241020a0.

[14] Chow, M. and Zukoski, C. Gold Sol Formation Mechanisms: Role of Colloidal Stability. *Journal of Colloid and Interface Science*, 165 (1), **1994**, pp. 97–109. doi:10.1006/jcis.1994.1210.

[15] Brust, M., Walker, M., Bethell, D., Schiffrin, D. J., and Whyman, R. Synthesis of thiol-derivatised gold nanoparticles in a two-phase Liquid-Liquid system. *Journal of the Chemical Society, Chemical Communications*, 7, **1994**, pp. 801–802. doi:10.1039/C39940000801.

[16] Saha, K., Agasti, S. S., Kim, C., Li, X., and Rotello, V. M. Gold Nanoparticles in Chemical and Biological Sensing. *Chemical Reviews*, 112 (5), **2012**, pp. 2739–2779. doi:10.1021/cr2001178.

[17] Zanoli, L., D'Agata, R., and Spoto, G. Functionalized gold nanoparticles for ultrasensitive DNA detection. *Analytical and Bioanalytical Chemistry*, 402 (5), **2012**, pp. 1759–1771. doi:10.1007/s00216-011-5318-3.

[18] Grzelczak, M., Perez-Juste, J., Mulvaney, P., and Liz-Marzan, L. M. Shape control in gold nanoparticle synthesis. *Chemical Society Reviews*, 37, **2008**, pp. 1783–1791. doi:10.1039/B711490G.

[19] Buffat, P.-A., Flueli, M., Spycher, R., Stadelmann, P., and Borel, J.-P. Crystallographic structure of small gold particles studied by high-resolution electron microscopy. *Faraday Discussions*, 92, **1991**, pp. 173–187. doi:10.1039/FD9919200173.

[20] Lee, Z., Jeon, K.-J., Dato, A., Erni, R., Richardson, T. J., Frenklach, M., and Radmilovic, V. Direct Imaging of Soft-Hard Interfaces Enabled by Graphene. *Nano Letters*, 9 (9), **2009**, pp. 3365–3369. doi:10.1021/nl901664k.

[21] Pashley, R. and Karaman, M. *Applied Colloid and Surface Chemistry*. Wiley, 2004, p. 109. ISBN 9780470868829.

[22] Bousse, L., Mostarshed, S., Shoot, B. V. D., de Rooij, N., Gimmel, P., and Göpel, W. Zeta potential measurements of Ta2O5 and SiO2 thin films. *Journal of Colloid and Interface Science*, 147 (1), **1991**, pp. 22–32. doi:10.1016/0021-9797(91)90130-Z.

[23] Kosmulski, M. and Matijevic, E. Zeta-potentials of silica in water-alcohol mixtures. *Langmuir*, 8 (4), **1992**, pp. 1060–1064. doi:10.1021/la00040a008.

[24] Scales, P. J., Grieser, F., Healy, T. W., White, L. R., and Chan, D. Y. C. Electrokinetics of the silica-solution interface: a flat plate streaming potential study. *Langmuir*, 8 (3), **1992**, pp. 965–974. doi:10.1021/la00039a037.

[25] Schwer, C. and Kenndler, E. Electrophoresis in fused-silica capillaries: the influence of organic solvents on the electroosmotic velocity and the .zeta. potential. *Analytical Chemistry*, 63 (17), **1991**, pp. 1801–1807. doi:10.1021/ac00017a026.

[26] Alvarez-Puebla, R. A., Arceo, E., Goulet, P. J. G., Garrido, J. J., and Aroca, R. F. Role of Nanoparticle Surface Charge in Surface-Enhanced Raman Scattering. *The Journal of Physical Chemistry B*, 109 (9), **2005**, pp. 3787–3792. doi:10.1021/jp045015o.

[27] Kunze, J., Burgess, I., Nichols, R., Buess-Herman, C., and Lipkowski, J. Electrochemical evaluation of citrate adsorption on Au(111) and the stability of citrate-reduced gold colloids. *Journal of Electroanalytical Chemistry*, 599 (2), **2007**, pp. 147 – 159. doi:10.1016/j.jelechem.2005.12.020.

[28] Malvern Instruments Ltd. *Zetasizer Nano series technical note - Zeta potential*, 2006. Available on-line: www.malwern.co.uk.

[29] Li, H. and Rothberg, L. Colorimetric detection of DNA sequences based on electrostatic interactions with unmodified gold nanoparticles. *Proceedings of the National Academy of Sciences of the United States of America*, 101 (39), **2004**, pp. 14036–14039. doi:10.1073/pnas.0406115101.

[30] Ojea-Jiménez, I., López, X., Arbiol, J., and Puntes, V. Citrate-Coated Gold Nanoparticles As Smart Scavengers for Mercury(II) Removal from Polluted Waters. *ACS Nano*, 6 (3), **2012**, pp. 2253–2260. doi:10.1021/nn204313a.

[31] Paciotti, G. F., Myer, L., Weinreich, D., Goia, D., Pavel, N., McLaughlin, R. E., and Tamarkin, L. Colloidal Gold: A Novel Nanoparticle Vector for Tumor Directed Drug Delivery. *Drug Delivery*, 11 (3), **2004**, pp. 169–183. doi:10.1080/10717540490433895.

[32] Reinhardt, K. and Kern, W. *Handbook of Silicon Wafer Cleaning Technology, 2nd Edition*. William Andrew, 2008, p. 186. ISBN 9780080947464.

[33] Pokrovsky, O., Golubev, S., and Mielczarski, J. Kinetic evidences of the existence of positively charged species at the quartz-aqueous solution interface. *Journal of Colloid and Interface Science*, 296 (1), **2006**, pp. 189–194. doi:10.1016/j.jcis.2005.09.001.

[34] Morita, M., Ohmi, T., Hasegawa, E., Kawakami, M., and Ohwada, M. Growth of native oxide on a silicon surface. *Journal of Applied Physics*, 68 (3), **1990**, pp. 1272–1281. doi:10.1063/1.347181.

[35] Li, H., Lin, Z., Wu, Z., and Lusk, M. T. First principles analysis of the initial oxidation of Si(001) and Si(111) surfaces terminated with H and CH_3. *The Journal of Chemical Physics*, 136 (6), **2012**, p. 064507. doi:10.1063/1.3682782.

[36] Panoiu, N.-C. and Osgood, R. M. Subwavelength Nonlinear Plasmonic Nanowire. *Nano Letters*, 4 (12), **2004**, pp. 2427–2430. doi:10.1021/nl048477m.

[37] Thyagarajan, K., Butet, J., and Martin, O. J. F. Augmenting Second Harmonic Generation Using Fano Resonances in Plasmonic Systems. *Nano Letters*, 13 (4), **2013**, pp. 1847–1851. doi:10.1021/nl400636z.

[38] Lalander, C. H., Zheng, Y., Dhuey, S., Cabrini, S., and Bach, U. DNA-Directed Self-Assembly of Gold Nanoparticles onto Nanopatterned Surfaces: Controlled Placement of Individual Nanoparticles into Regular Arrays. *ACS Nano*, 4 (10), **2010**, pp. 6153–6161. doi:10.1021/nn101431k.

[39] Palleau, E., Sangeetha, N. M., Viau, G., Marty, J.-D., and Ressier, L. Coulomb Force Directed Single and Binary Assembly of Nanoparticles from Aqueous Dispersions by AFM Nanoxerography. *ACS Nano*, 5 (5), **2011**, pp. 4228–4235. doi:10.1021/nn2011893.

[40] Fan, J. A., Bao, K., Sun, L., Bao, J., Manoharan, V. N., Nordlander, P., and Capasso, F. Plasmonic Mode Engineering with Templated Self-Assembled Nanoclusters. *Nano Letters*, 12 (10), **2012**, pp. 5318–5324. doi:10.1021/nl302650t.

[41] Onclin, S., Ravoo, B. J., and Reinhoudt, D. N. Engineering Silicon Oxide Surfaces Using Self-Assembled Monolayers. *Angewandte Chemie International Edition*, 44 (39), **2005**, pp. 6282–6304. doi:10.1002/anie.200500633.

[42] Mendes, P. M., Jacke, S., Critchley, K., Plaza, J., Chen, Y., Nikitin, K., Palmer, R. E., Preece, J. A., Evans, S. D., and Fitzmaurice, D. Gold Nanoparticle Patterning of Silicon Wafers Using Chemical e-Beam Lithography. *Langmuir*, 20 (9), **2004**, pp. 3766–3768. doi:10.1021/la049803g.

[43] Jiang, L., Sun, Y., Nowak, C., Kibrom, A., Zou, C., Ma, J., Fuchs, H., Li, S., Chi, L., and Chen, X. Patterning of Plasmonic Nanoparticles into Multiplexed One-Dimensional Arrays Based on Spatially Modulated Electrostatic Potential. *ACS Nano*, 5 (10), **2011**, pp. 8288–8294. doi:10.1021/nn202967f.

[44] Onses, M. S., Pathak, P., Liu, C.-C., Cerrina, F., and Nealey, P. F. Localization of Multiple DNA Sequences on Nanopatterns. *ACS Nano*, 5 (10), **2011**, pp. 7899–7909. doi:10.1021/nn2021277.

[45] Tzeng, S.-D., Lin, K.-J., Hu, J.-C., Chen, L.-J., and Gwo, S. Templated Self-Assembly of Colloidal Nanoparticles Controlled by Electrostatic Nanopatterning on a Si3N4/SiO2/Si Electret. *Advanced Materials*, 18 (9), **2006**, pp. 1147–1151. doi:10.1002/adma.200501542.

[46] Lee, I., Zheng, H., Rubner, M., and Hammond, P. Controlled Cluster Size in Patterned Particle Arrays via Directed Adsorption on Confined Surfaces. *Advanced Materials*, 14 (8), **2002**, pp. 572–577. doi:10.1002/1521-4095(20020418)14:8<572::AID-ADMA572>3.0.CO;2-B.

[47] Cui, Y., Björk, M. T., Liddle, J. A., Sönnichsen, C., Boussert, B., and Alivisatos, A. P. Integration of Colloidal Nanocrystals into Lithographically Patterned Devices. *Nano Letters*, 4 (6), **2004**, pp. 1093–1098. doi:10.1021/nl049488i.

[48] Utke, I., Hoffmann, P., and Melngailis, J. Gas-assisted focused electron beam and ion beam processing and fabrication. *Journal of Vacuum Science and Technology B*, 26 (4), **2008**, pp. 1197–1276. doi:10.1116/1.2955728.

[49] Mie, G. Beiträge zur Optik trüber Medien, speziell kolloidaler Metallösungen. *Annalen der Physik*, 330 (3), **1908**, pp. 377–445. doi:10.1002/andp.19083300302. English translation available at http://diogenes.iwt.uni-bremen.de/vt/laser/papers/RAE-LT1873-1976-Mie-1908-translation.pdf [Accesed 24 May 2013].

[50] Jackson, J. D. *Classical Electrodynamics, 3rd Edition*. Wiley, 1998, p. 159. ISBN 9780471309321.

[51] Bohren, C. F. and Huffman, D. *Absorption and scattering of light by small particles*. Wiley, 1983, p. 140. ISBN 9780471293408. doi:10.1002/9783527618156.

[52] Alvarez-Puebla, R. A. and Liz-Marzán, L. M. SERS-Based Diagnosis and Biodetection. *Small*, 6 (5), **2010**, pp. 604–610. doi:10.1002/smll.200901820.

[53] Stiles, P. L., Dieringer, J. A., Shah, N. C., and Van Duyne, R. P. Surface-Enhanced Raman Spectroscopy. *Annual Review of Analytical Chemistry*, 1 (1), **2008**, pp. 601–626. doi:10.1146/annurev.anchem.1.031207.112814.

[54] Link, S. and El-Sayed, M. A. Size and Temperature Dependence of the Plasmon Absorption of Colloidal Gold Nanoparticles. *The Journal of Physical Chemistry B*, 103 (21), **1999**, pp. 4212–4217. doi:10.1021/jp984796o.

[55] Kreibig, U. and Vollmer, M. *Optical properties of metal clusters*. Springer, 1995, p. 76. ISBN 9780387578361.

[56] Barber, P. and Chang, R. (eds.). *Optical effects associated with small particles*. World Scientific, 1988, p. 279. ISBN 9789971504625.

[57] Willets, K. A. and Van Duyne, R. P. Localized Surface Plasmon Resonance Spectroscopy and Sensing. *Annual Review of Physical Chemistry*, 58 (1), **2007**, pp. 267–297. doi:10.1146/annurev.physchem.58.032806.104607.

[58] Lee, K.-S. and El-Sayed, M. A. Dependence of the Enhanced Optical Scattering Efficiency Relative to That of Absorption for Gold Metal Nanorods on Aspect Ratio, Size,

End-Cap Shape, and Medium Refractive Index. *The Journal of Physical Chemistry B*, 109 (43), **2005**, pp. 20331–20338. doi:10.1021/jp054385p.

[59] Hao, F. and Nordlander, P. Efficient dielectric function for FDTD simulation of the optical properties of silver and gold nanoparticles. *Chemical Physics Letters*, 446, **2007**, pp. 115 – 118. doi:10.1016/j.cplett.2007.08.027.

[60] Adams, S. M., Campione, S., Capolino, F., and Ragan, R. Directing Cluster Formation of Au Nanoparticles from Colloidal Solution. *Langmuir*, 29 (13), **2013**, pp. 4242–4251. doi:10.1021/la3051719.

[61] Zhao, J., Pinchuk, A. O., McMahon, J. M., Li, S., Ausman, L. K., Atkinson, A. L., and Schatz, G. C. Methods for Describing the Electromagnetic Properties of Silver and Gold Nanoparticles. *Accounts of Chemical Research*, 41 (12), **2008**, pp. 1710–1720. doi:10.1021/ar800028j.

[62] Eustis, S. and El-Sayed, M. A. Why gold nanoparticles are more precious than pretty gold: Noble metal surface plasmon resonance and its enhancement of the radiative and nonradiative properties of nanocrystals of different shapes. *Chemical Society Reviews*, 35, **2006**, pp. 209–217. doi:10.1039/B514191E.

[63] Huang, X., Neretina, S., and El-Sayed, M. A. Gold Nanorods: From Synthesis and Properties to Biological and Biomedical Applications. *Advanced Materials*, 21 (48), **2009**, pp. 4880–4910. doi:10.1002/adma.200802789.

[64] Ghosh, S. K. and Pal, T. Interparticle Coupling Effect on the Surface Plasmon Resonance of Gold Nanoparticles: From Theory to Applications. *Chemical Reviews*, 107 (11), **2007**, pp. 4797–4862. doi:10.1021/cr0680282.

[65] Romero, I., Aizpurua, J., Bryant, G. W., and Abajo, F. J. G. D. Plasmons in nearly touching metallic nanoparticles: singular response in the limit of touching dimers. *Optics Express*, 14 (21), **2006**, pp. 9988–9999. doi:10.1364/OE.14.009988.

[66] Barrow, S. J., Funston, A. M., Wei, X., and Mulvaney, P. DNA-directed self-assembly and optical properties of discrete 1D, 2D and 3D plasmonic structures. *Nano Today*, 8 (2), **2013**, pp. 138–167. doi:10.1016/j.nantod.2013.02.005.

[67] Fan, J. A., Wu, C., Bao, K., Bao, J., Bardhan, R., Halas, N. J., Manoharan, V. N., Nordlander, P., Shvets, G., and Capasso, F. Self-Assembled Plasmonic Nanoparticle Clusters. *Science*, 328 (5982), **2010**, pp. 1135–1138. doi:10.1126/science.1187949.

[68] Antosiewicz, T. J., Apell, S. P., Zäch, M., Zorić, I., and Langhammer, C. Oscillatory Optical Response of an Amorphous Two-Dimensional Array of Gold Nanoparticles. *Physical Review Letters*, 109, **2012**, p. 247401. doi:10.1103/PhysRevLett.109.247401.

[69] Geiregat, P., Justo, Y., Abe, S., Flamee, S., and Hens, Z. Giant and Broad-Band Absorption Enhancement in Colloidal Quantum Dot Monolayers through Dipolar Coupling. *ACS Nano*, 7 (2), **2013**, pp. 987–993. doi:10.1021/nn305524a.

[70] Weick, G., Woollacott, C., Barnes, W. L., Hess, O., and Mariani, E. Dirac-like Plasmons in Honeycomb Lattices of Metallic Nanoparticles. *Physical Review Letters*, 110, **2013**, p. 106801. doi:10.1103/PhysRevLett.110.106801.

[71] Hsu, S.-H., Chang, Y.-C., Chen, Y.-C., Wei, P.-K., and Kim, Y. D. Optical metrology of randomly-distributed Au colloids on a multilayer film. *Optics Express*, 18 (2), **2010**, pp. 1310–1315. doi:10.1364/OE.18.001310.

[72] Humlicek, J. Data Analysis for Nanomaterials: Effective Medium Approximation, Its Limits and Implementations. In M. Losurdo and K. Hingerl (eds.), *Ellipsometry at the Nanoscale*, pp. 145–178. Springer, 2013. ISBN 978-3-642-33955-4. doi:10.1007/978-3-642-33956-1_3.

[73] Fujiwara, H. *Spectroscopic Ellipsometry*. Wiley Blackwell (John Wiley & Sons), 2007, p. 177. ISBN 9780470060193. doi:10.1002/9780470060193.

[74] Azzam, R. and Bashara, N. *Ellipsometry and polarized light*. North-Holland Pub. Co., 1977, p. 1. ISBN 9780444870162.

[75] Ligmajer, F. *Deposition of Metal Nanoparticles from Solution and Study of Their Optical Properties. (In Czech)*. Master's thesis, Brno University of Technology, Faculty of Mechanical Engineering, 2011.

[76] Henrion, W., Rebien, M., Angermann, H., and Röseler, A. Spectroscopic investigations of hydrogen termination, oxide coverage, roughness, and surface state density of silicon during native oxidation in air. *Applied Surface Science*, 202, **2002**, pp. 199–205. doi:10.1016/S0169-4332(02)00923-6.

[77] J. A. Woollam Co., Inc. *Guide to Using WVASE32*, 2010. p. 7-37.

[78] Garnett, J. C. M. Colours in Metal Glasses and in Metallic Films. *Philosophical Transactions of the Royal Society of London*, 203, **1904**, pp. 385–420. doi:10.1098/rsta.1904.0024.

[79] Kooij, E. S., Wormeester, H., Brouwer, E. A. M., van Vroonhoven, E., van Silfhout, A., and Poelsema, B. Optical Characterization of Thin Colloidal Gold Films by Spectroscopic Ellipsometry. *Langmuir*, 18 (11), **2002**, pp. 4401–4413. doi:10.1021/la0256127.

[80] Brolo, A. G. Plasmonics for future biosensors. *Nature Photonics*, 6 (11), **2012**, pp. 709–713. doi:10.1038/nphoton.2012.266.

[81] Maier, S. A. *Plasmonics: Fundamentals and Applications*. Springer, 2007. ISBN 9780387378251. doi:10.1007/0-387-37825-1.

[82] Homola, J., Yee, S. S., and Gauglitz, G. Surface plasmon resonance sensors: review. *Sensors and Actuators B: Chemical*, 54, **1999**, pp. 3–15. doi:10.1016/S0925-4005(98)00321-9.

[83] Read, T., Olkhov, R. V., and Shaw, A. M. Measurement of the localised plasmon penetration depth for gold nanoparticles using a non-invasive bio-stacking method. *Physical Chemistry Chemical Physics*, 15, **2013**, pp. 6122–6127. doi:10.1039/C3CP50758K.

[84] Haes, A. J., Zou, S., Zhao, J., Schatz, G. C., and Van Duyne, R. P. Localized Surface Plasmon Resonance Spectroscopy near Molecular Resonances. *Journal of the American Chemical Society*, 128 (33), **2006**, pp. 10905–10914. doi:10.1021/ja063575q.

[85] Sherry, L. J., Jin, R., Mirkin, C. A., Schatz, G. C., and Van Duyne, R. P. Localized Surface Plasmon Resonance Spectroscopy of Single Silver Triangular Nanoprisms. *Nano Letters*, 6 (9), **2006**, pp. 2060–2065. doi:10.1021/nl061286u.

[86] Raschke, G., Kowarik, S., Franzl, T., Sönnichsen, C., Klar, T. A., Feldmann, J., Nichtl, A., and Kürzinger, K. Biomolecular Recognition Based on Single Gold Nanoparticle Light Scattering. *Nano Letters*, 3 (7), **2003**, pp. 935–938. doi:10.1021/nl034223+.

[87] Sapsford, K. E., Algar, W. R., Berti, L., Gemmill, K. B., Casey, B. J., Oh, E., Stewart, M. H., and Medintz, I. L. Functionalizing Nanoparticles with Biological Molecules: Developing Chemistries that Facilitate Nanotechnology. *Chemical Reviews*, 113 (3), **2013**, pp. 1904–2074. doi:10.1021/cr300143v.

[88] Katz, E. and Willner, I. Integrated Nanoparticle–Biomolecule Hybrid Systems: Synthesis, Properties, and Applications. *Angewandte Chemie International Edition*, 43 (45), **2004**, pp. 6042–6108. doi:10.1002/anie.200400651.

[89] Daniel, M.-C. and Astruc, D. Gold Nanoparticles: Assembly, Supramolecular Chemistry, Quantum-Size-Related Properties, and Applications toward Biology, Catalysis, and Nanotechnology. *Chemical Reviews*, 104 (1), **2004**, pp. 293–346. doi:10.1021/cr030698+.

[90] Li, P., Li, D., Zhang, L., Li, G., and Wang, E. Cationic lipid bilayer coated gold nanoparticles-mediated transfection of mammalian cells. *Biomaterials*, 29 (26), **2008**, pp. 3617–3624. doi:10.1016/j.biomaterials.2008.05.020.

[91] Biju, V., Itoh, T., Anas, A., Sujith, A., and Ishikawa, M. Semiconductor quantum dots and metal nanoparticles: syntheses, optical properties, and biological applications. *Analytical and Bioanalytical Chemistry*, 391 (7), **2008**, pp. 2469–2495. doi:10.1007/s00216-008-2185-7.

[92] Love, J. C., Estroff, L. A., Kriebel, J. K., Nuzzo, R. G., and Whitesides, G. M. Self-Assembled Monolayers of Thiolates on Metals as a Form of Nanotechnology. *Chemical Reviews*, 105 (4), **2005**, pp. 1103–1170. doi:10.1021/cr0300789.

[93] El-Deiry, W. S., Kern, S. E., Pietenpol, J. A., Kinzler, K. W., and Vogelstein, B. Definition of a consensus binding site for p53. *Nature Genetics*, 1 (1), **1992**, pp. 45–49.

[94] Hurst, S. J., Lytton-Jean, A. K. R., and Mirkin, C. A. Maximizing DNA Loading on a Range of Gold Nanoparticle Sizes. *Analytical Chemistry*, 78 (24), **2006**, pp. 8313–8318. doi:10.1021/ac0613582.

[95] Zhang, X., Servos, M. R., and Liu, J. Surface Science of DNA Adsorption onto Citrate-Capped Gold Nanoparticles. *Langmuir*, 28 (8), **2012**, pp. 3896–3902. doi:10.1021/la205036p.

[96] Saleh, B. and Teich, M. *Fundamentals of Photonics*. Wiley, 2007, p. 179. ISBN 9780471358329. doi:10.1002/0471213748.

LIST OF ABBREVIATIONS

Acronym	Meaning
AuNP	Gold Nanoparticle
BEMA	Bruggeman's Effective Medium Approximation
DDA	Discrete Dipole Approximation
DNA	Deoxyribonucleic Acid
EBL	Electron Beam Lithography
EMA	Effective Medium Approximation
FDTD	Finite-difference Time-domain
FEM	Finite Element Method
FTIR	Fourier Transform Infrared
KK	Kramers-Kronig
LSPR	Localised Surface Plasmon Resonance
MG	Maxwell Garnett
MSE	Mean Squared Error
SEM	Scanning Electron Microscope
SERS	Surface-enhanced Raman Spectroscopy
SPP	Surface Plasmon Polariton
SPR	Surface Plasmon Resonance
TEM	Transmission Electron Microscope

A REFRACTIVE INDEX OF GOLD USED IN ELLIPSOMETRY FITTING

Tab. A.1: Real and imaginary part of the refractive index of gold, which was used for ellipsometric spectra fitting (results are shown in Figure 3.7). Material constants were measured at J. A. Woollam, Co., and provided as a part of the VASE ellipsometer software.

Wavelength (nm)	n	k	Wavelength (nm)	n	k
390	1.6254	2.0526	700	0.2021	4.3139
400	1.6208	2.0612	710	0.2026	4.4112
410	1.6115	2.0630	720	0.2036	4.5058
420	1.5948	2.0596	730	0.2044	4.5968
430	1.5705	2.0520	740	0.2049	4.6898
440	1.5371	2.0394	750	0.2075	4.7810
450	1.4917	2.0210	760	0.2109	4.8698
460	1.4296	1.9980	770	0.2135	4.9600
470	1.3446	1.9729	780	0.2163	5.0474
480	1.2278	1.9566	790	0.2193	5.1327
490	1.0815	1.9669	800	0.2206	5.2194
500	0.9198	2.0244	810	0.2247	5.3072
510	0.7714	2.1295	820	0.2277	5.3913
520	0.6544	2.2587	830	0.2303	5.4762
530	0.5657	2.3945	840	0.2330	5.5595
540	0.4968	2.5319	850	0.2364	5.6473
550	0.4436	2.6651	860	0.2404	5.7277
560	0.4001	2.7936	870	0.2433	5.8105
570	0.3645	2.9186	880	0.2459	5.8917
580	0.3358	3.0390	890	0.2460	5.9723
590	0.3113	3.1565	900	0.2495	6.0561
600	0.2915	3.2704	910	0.2555	6.1370
610	0.2733	3.3840	920	0.2579	6.2205
620	0.2589	3.4927	930	0.2603	6.3013
630	0.2461	3.5996	940	0.2654	6.3788
640	0.2347	3.7067	950	0.2668	6.4607
650	0.2250	3.8114	960	0.2670	6.5410
660	0.2174	3.9150	970	0.2783	6.6194
670	0.2121	4.0172	980	0.2761	6.6996
680	0.2071	4.1174	990	0.2775	6.7788
690	0.2053	4.2176	1000	0.2820	6.8529